KTH ROYAL INSTITUTE
OF TECHNOLOGY

Doctoral Thesis in Civil and Architectural Engineering

Modeling aspects of reliability-based design of lined rock caverns

DAVI RODRIGUES DAMASCENO

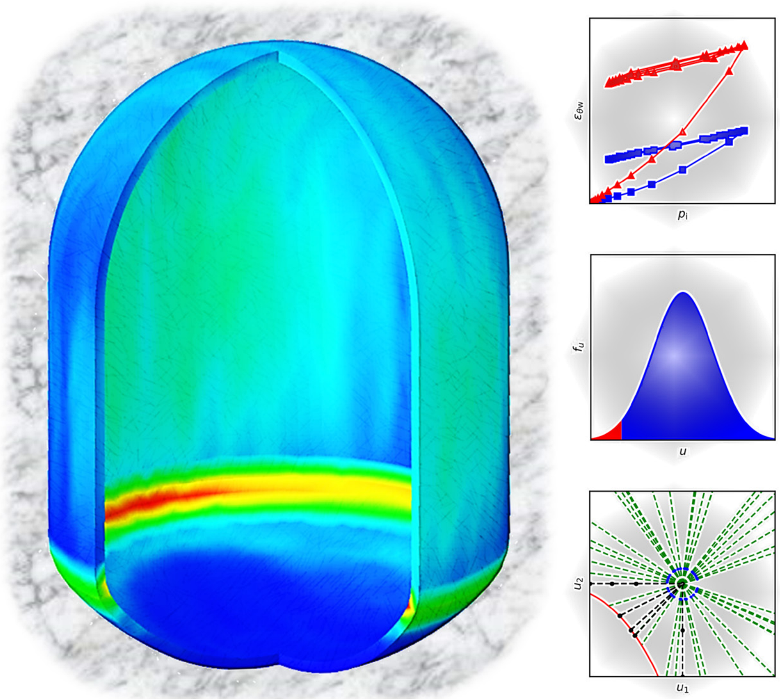

Stockholm, Sweden 2022

Modeling aspects of reliability-based design of lined rock caverns

DAVI RODRIGUES DAMASCENO

Academic Dissertation which, with due permission of the KTH Royal Institute of Technology, is submitted for public defence for the Degree of Doctor of Philosophy on Friday the 2nd December 2022, at 1:00 p.m. in D2, Lindstedtsvägen 9, Stockholm.

Doctoral Thesis in Civil and Architectural Engineering
KTH Royal Institute of Technology
Stockholm, Sweden 2022

TRITA-ABE-DLT-2242
ISBN 978-91-8040-404-4

Printed by: Universitetsservice US-AB, Sweden 2022

Abstract

The storage of large quantities of hydrogen gas in underground lined rock caverns (LRCs) could contribute to an efficient supply of fossil-free energy. The consequences of failure of such storage can be catastrophic, so representative predictive models and a small probability of failure are needed for the LRC design. However, the available predictive models are simplified. On top of that, the calculation of a small probability of failure is challenging on its own, and becomes more difficult when combined with representative numerical models, which are often computationally demanding.

The purpose of this thesis is to develop a reliability-based design tool for LRC gas storages to ensure that societal safety requirements are met. For the development of this LRC design tool, the research issues are related to the prediction of the rock cavern response to a high internal gas pressure; interaction between LRC components; suitability of reliability-based calculation methods for the LRC design; and, effect of uncertainties on the probability of failure of the LRC design.

The results show that the available analytical model to predict the rock cavern response is only applicable for idealized geological conditions and geometries, so numerical models are needed. Finite element (FE) models are therefore developed to account for the complex interaction between LRC components, including the influence of opening of discrete rock joints on the strain concentrations in the steel lining. The adaptive directional importance sampling (ADIS) method is identified to be suitable to perform reliability-based analysis with FE models, requiring only a small number of samples for sufficiently accurate estimations of small probabilities of failure. The structural reliability of the LRC design is found to be sensitive to the rock mass quality and the correlation between geological properties.

Keywords

Lined rock cavern, reliability-based design, analytical modeling, finite element modeling, underground gas storage

Sammanfattning

Lagring av stora mängder vätgas i underjordiska inklädda bergrum (LRC) skulle kunna bidra till en effektiv försörjning av fossilfri energi. Konsekvenserna av läckage i sådana lager kan vara katastrofala, så bra beräkningsmodeller behövs för att kunna verifiera att brottsannolikheten i LRC är tillräckligt liten. De tillgängliga beräkningsmodellerna är dock förenklade. Dessutom är beräkningen av små brottsannolikheter utmanande i sig och blir ännu svårare i kombination med representativa numeriska modeller, eftersom sådana modeller kräver långa beräkningstider.

Syftet med denna doktorsavhandling är att utveckla ett sannlikhetsbaserat designverktyg för att uppfylla de säkerhetskrav som ställs vid lagring av trycksatt gas i LRC. De specifika forskningsfrågorna är relaterade till modellerandet av bergrummets mekaniska beteende; interaktionen mellan LRC-komponenter; lämpligheten av sannolikhetsbaserade beräkningsmetoder för LRC-designen; samt effekten av osäkerheter på sannolikheten för brott i LRC-designen.

Resultaten visar att den befintliga analytiska modellen för att modellera bergrummets beteende endast är tillämpbar för idealiserade geologiska förhållanden och geometrier, vilket indikerar att numeriska modeller behövs. Sådana modeller har därför utvecklats för att ta hänsyn till interaktionen mellan LRC-komponenter, vilka beaktar hur öppning av bergssprickor påverkar stålinklädnadens töjning. Den adaptiva riktade viktningssamplingsmetoden (ADIS) har identifierats vara lämplig för att utföra sannolikhetsbaserade analyser med FE-modellerna, eftersom ADIS kan ge tillräckligt exakta uppskattningar av små brottsannolikheter trots få körningar av den numeriska modellen. Brottsannolikhetsberäkningarna har visat sig vara känsliga för främst bergmassans kvalitet och korrelationen mellan geologiska egenskaper.

Nyckelord

Inklädda bergrum, tillförlitlighetsbaserad design, analytisk modellering, finita elementmodellering, underjordisk gaslagring

Preface

The research presented in this doctoral thesis was carried out between the end of 2017 and the end of 2022 at the Division of Soil and Rock Mechanics, Department of Civil and Architectural Engineering, at KTH Royal Institute of Technology in Stockholm, Sweden.

Dr. Fredrik Johansson, Dr. Johan Spross, and Prof. Stefan Larsson supervised this work and I thank them for their great support and contributions. I am grateful for the valuable discussions I had with the group of experts composed by Prof. Håkan Stille (KTH), Jan Johansson (Naturgasteknik), Per Tengborg (BeFo), and Robert Sturk (Skanska). I also thank Bojan Stojanovic (Vattenfall), Nicklas Simonsson (Vattenfall), Marie Anheden (Vattenfall), Märit Berglind Eriksson (Sweco), and Jennifer Hellberg (Itasca), who were part of an industry reference group.

I would like to thank my colleagues and friends in KTH for the interesting discussions and nice after works. I'm grateful for the love and moral support of my family, especially my mom Wólnea, dad José Eustáquio, and brother Tomás, which gave me the strength to pursue my dreams in a foreign country. And thanks to those who became my family and made me feel home far away from where I was born.

Stockholm, November 2022

Davi Rodrigues Damasceno

Funding acknowledgement

This work was financially supported by the Swedish Energy Agency [grant numbers 42684-2 and P2022-00209]. It was part of the HYBRIT research project RP-1, Work Package 2.3, which aimed to further develop the LRC concept for large-scale underground storage of hydrogen gas.

List of appended papers

This doctoral thesis is based upon the following scientific articles. The scientific papers here are in the order of development of LRC models (Papers A and B), suitability of reliability-based calculation methods for the LRC design (Papers C and D), and reliability-based analysis for LRCs (Paper E).

Paper A

Damasceno, D. R., Spross, J., and Johansson, F., 2022. Rock mass response for lined rock caverns subjected to high internal gas pressure. Journal of Rock Mechanics and Geotechnical Engineering. In press.

Damasceno derived the analytical model, constructed the finite element model, performed the calculations, and wrote the paper. Spross and Johansson assisted with comments on the figures and writing.

Paper B

Damasceno, D. R., Spross, J., and Johansson, F., 2022. Strain concentrations in lined rock caverns subjected to internal gas pressure: effects of rock joints. Resubmitted after revision to Journal of Rock Mechanics and Geotechnical Engineering.

Damasceno derived the analytical model, constructed the finite element model, performed the calculations, and wrote the paper. Spross and Johansson assisted with comments on the figures and writing.

Paper C

Damasceno, D. R., Spross, J., Johansson, F., and Johansson, J., 2019. Efficiency of subset simulation in the design of lined rock caverns for storage of hydrogen gas. Proceedings of the 13th International Conference on Applications of Statistics and Probability in Civil Engineering, ID 124, Seoul, South Korea.

Damasceno performed the calculations and wrote the paper. Spross helped with the subset simulation method. Spross and Johansson, F., assisted with comments on the figures and writing. Johansson, J., assisted with consulting experience regarding the LRC concept.

Paper D

Damasceno, D. R., Spross, J., and Johansson, F., 2020. Reliability-based design methodology for lined rock cavern depth using the response surface method. Proceeding of the ISRM International Symposium - EUROCK 2020, ID 163, Trondheim, Norway.

Damasceno derived the analytical model, performed the calculations, and wrote the paper. Spross and Johansson assisted with comments on the figures and writing.

Paper E

Damasceno, D. R., Spross, J., and Johansson, F., 2022. Reliability-based design tool for gas storage in lined rock caverns. Submitted to Georisk: Assessment and Management of Risk for Engineered Systems and Geohazards.

Damasceno constructed the finite element model, performed the calculations, and wrote the paper. Spross and Johansson assisted with comments on the figures and writing.

Other publications

Within the framework of this research project, I also contributed to the following publications (not included in this thesis).

Johansson, F., Spross, J., **Damasceno, D. R.**, Johansson, J., and Stille, H., 2018. Investigation of research needs regarding the storage of hydrogen gas in lined rock caverns: pre-study for work package 2.3 in HYBRIT research program 1. TRITA-ABE-RPT-182. KTH Royal Institute of Technology, Stockholm, Sweden.

Spross, J., **Damasceno, D. R.**, Johansson, F., Johansson, J., Stojanovic, B., and Simomsson, N., 2019. Storskalig lagring av vätgas i bergrum [Large-scale storage of hydrogen gas in rock caverns]. Bygg & Teknik, 1/19.

Contents

1. Introduction 1
1.1. Background 1
1.2. Aim of the thesis 4
1.3. Research methodology 5
1.4. Outline of thesis 6
1.5. Limitations 6

2. Modeling of the lined rock cavern 7
2.1. Geometry 7
2.2. In-situ stresses 9
2.3. Gas pressure and temperature 11
2.4. Rock mass properties 16
2.5. Lining properties 20
2.5.1. Concrete material 21
2.5.2. Steel material 22
2.5.3. Contact interactions 23

3. Structural response of the lined rock cavern 25
3.1. Excavation of the rock cavern 25
3.2. Failure of the steel lining 27
3.3. Uplifting of the overburden rock mass 29
3.4. Tangential strains at the rock cavern wall 31
3.5. Steel lining strain concentrations at concrete cracks 36
3.6. Thermal strains at the steel lining 39

4. Modeling of uncertainties 41
4.1. Sources of uncertainty 41
4.2. Description of uncertain properties 42
4.3. Correlation and distribution transformations 44
4.4. Spatial variability 46

5. Reliability-based analysis 49
5.1. Structural reliability 49
5.2. Acceptable probability of failure 51

5.3. Performance functions....................52
5.3.1. Uplifting of the overburden rock mass....................52
5.3.2. Ultimate straining of the steel lining....................53
5.3.3. Fatigue of the steel lining....................54
5.4. Reliability calculation methods....................54
5.4.1. Monte Carlo simulation....................57
5.4.2. Directional simulation....................57
5.4.3. Response surface method....................59
5.4.4. Subset simulation....................60
5.4.5. Adaptive directional importance sampling....................60

6. Summary of appended papers....................63
6.1. Paper A....................63
6.2. Paper B....................63
6.3. Paper C....................64
6.4. Paper D....................65
6.5. Paper E....................66

7. Discussion....................67
7.1. Development of lined rock cavern models....................67
7.1.1. Importance of the analytical model....................67
7.1.2. Complex interaction between lining components....................68
7.1.3. Modeling aspects for the advanced reliability-based design....................69
7.2. Reliability-based analysis....................69
7.2.1. Considerations for conventional methods....................69
7.2.2. Considerations for advanced methods....................71
7.3. Compliance with safety requirement....................72
7.3.1. Uplifting of the overburden....................72
7.3.2. Ultimate straining of the steel lining....................73
7.3.3. Fatigue of the steel lining....................74

8. Conclusions and suggestions for future work....................75
8.1. Conclusions....................75
8.2. Suggestions for future work....................77

References....................79

1. Introduction

1.1. Background

International efforts to make the energy matrix in society cleaner and more renewable include the potential substitution of fossil fuels by hydrogen gas. The process of water electrolysis produces hydrogen gas, which can be used as a combusting fuel, e.g. for automotive and domestic applications, with the release of water as a byproduct. An infrastructure capable of storing large quantities of hydrogen gas will however be needed to supply the societal energy demand.

One example of the infrastructural need for large-scale gas storages is the Hydrogen Breakthrough Ironmaking Technology (HYBRIT) initiative, which aims to implement in Sweden the first fossil-free steelmaking process. Fossil-fuels and coal that are conventionally used in several steps of the steelmaking value-chain are to be substituted by hydrogen gas and electricity. In the fossil-free process, the hydrogen gas can be used as an energy carrier in the electric arc furnace and in the process of direct reduction for sponge iron. Industrial quantities of hydrogen gas are to be produced and must be readily available in a large-scale storage to enable this alternative steelmaking process. For this purpose, an underground storage pilot plant with a volume of 100 m^3 was inaugurated in Luleå, Sweden (Vattenfall Press Office, 2022), using the lined rock cavern (LRC) concept. It is expected that an LRC of 100 000 m^3, filled with hydrogen gas, could supply up to 100 GWh of electricity, which would be sufficient for half a week operation of a full-scale sponge iron factory.

During the 1980s-1990s in Sweden, the LRC concept was developed as an underground solution for large-scale storage of gas (Stille et al., 1994, Lu, 1998, Johansson, 2003, Tengborg et al., 2014). A steel lining prevents gas leakage while the surrounding rock mass provides confinement against the internal pressure increase during gas filling of the storage. The LRC concept uses conventional excavation methods and civil engineering materials, and is reliable for geological conditions of hard rock masses. The LRC design principles were proposed based on pilot testing of three LRCs, of 100 m^3 each, in Grängesberg, Sweden, performed in the early 1990s. In 2002, an LRC of 40 000 m^3 was put into commercial operation for the storage of natural gas in Skallen, southwestern Sweden (Johansson 2003, Glamheden and Curtis 2006, Tengborg et al. 2014), where the rock mass is dominated by good-quality gneiss.

A full-scale LRC with its main components is shown in Figure 1.1. During construction, access tunnels and shafts are used to excavate the rock and steel plates are welded together inside the cavern. During the casting of the concrete in the annulus, the cavern is filled with water for stability of the steel lining. As a safety measure, a system of pipes is present for detection and drainage of any gas leakage. The concrete reinforcement and sliding layer aim to limit the cracking of the concrete layer and redistribute the strains close to the steel lining. However, large concrete

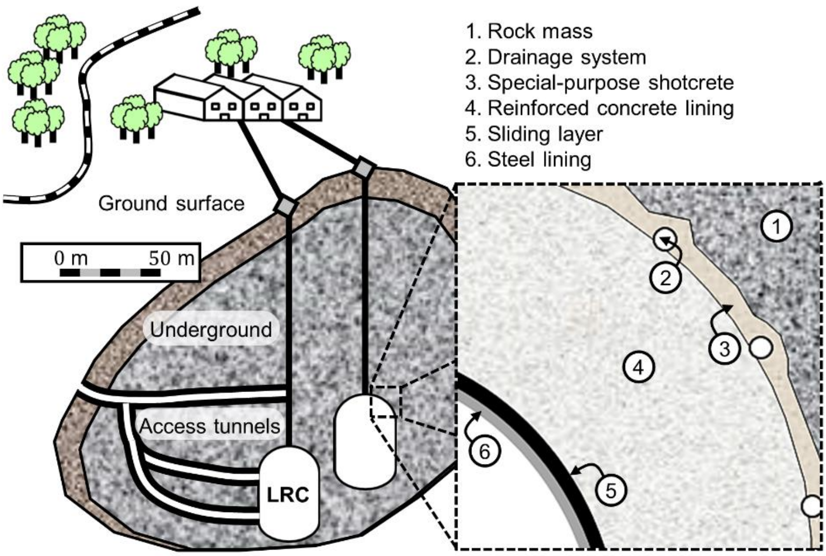

Figure 1.1. Sketch of the LRC concept, highlighting the main lining components.

cracks can still occur from the opening of rock joints at the cavern wall due to the gas pressurization. This can cause local concentrations of strains in the steel lining.

The LRC design must be able to prevent failure of the steel lining. Ultimate failure due to uplifting of the overlying rock mass is avoided by placing the LRC at sufficient depth. Then, the remaining critical failure mode is related to the fatigue of the steel lining due to repeated gas filling and emptying of the storage. It is important that the steel plates and welds in the lining have a sufficiently high quality to avoid rupturing of the lining caused by local defects. However, the current models to predict the LRC deformation behavior because of a high internal gas pressure (Lu, 1998, Johansson, 2003, Glamheden and Curtis, 2006, Park et al., 2013) are simplified, e.g., they do not account for the interaction between LRC components or details in the 3D geometry.

Finding suitable sites for the construction and operation of the LRC is another engineering challenge, since high design reliability is required, and there are prevailing uncertainties associated with the geological conditions at the considered site. Codes and regulations provide no specific guidelines for the LRC design. The traditional practice in civil engineering has been to use a deterministic safety factors to ensure structural safety, which implies a single safety margin to account for all uncertainties. However, a safety factor may not be calibrated against societal safety requirements since it is determined heuristically, i.e., based on previous design experiences over a long period of time. A more consistent approach is to use reliability-based assessments, where the uncertainties are accounted for explicitly. Reliability-based analysis assesses the probability of failure of a structural design and has been implemented successfully in many underground engineering applications; see, e.g., Kohno et al. (1992), Diederichs and Kaiser (1996), Celestino et al. (2006), Phoon (2008), Langford and Diederichs (2013), Lü et al. (2013), Zeng et al. (2016), Bjureland et al. (2017), and Spross et al. (2022). Conventional reliability-based analyses that consider the joint distribution of all uncertainties often require many evaluations of a design performance response, especially for small target probabilities of failure, which is the case for the LRC design.

Further model developments with respect to the complex interactions between LRC components and the cavern 3D geometry are needed to ensure that the LRC design meets the societal safety requirements. A tradeoff to consider is that more representative LRC design models become computationally demanding and take longer times to run. In combination with a requirement for many repeated model evaluations, this leads to unpractical computational times for the evaluation of small probabilities of failure and imposes an obstacle for the reliability-based design of LRCs. A suitable reliability-based method for computationally demanding models is needed in order to accurately estimate small probabilities of failure for the LRC design.

1.2. Aim of the thesis

The overall aim of this thesis is to ensure that the design of LRC gas storages meet societal safety requirements. For that, an LRC design tool combining advanced numerical models with probabilistic analysis needs to be developed. This would enable the reliability-based design of LRCs, accordingly addressing the uncertainties related to the rock mass to meet the storage demands for fossil-free energy.

The specific goal is to develop such a reliability-based design tool for LRCs. For that, the research questions that need to be answered are identified as:

1) What is the response behavior of a rock cavern to high internal gas pressure?

2) What is the specific interaction behavior between individual LRC components?

3) Which reliability-based calculation methods are suitable for the design of LRCs?

4) What is the effect of uncertainties on the probability of failure of the LRC design?

1.3. Research methodology

This work was initiated with a literature review for potential research questions regarding the storage of hydrogen gas in lined rock caverns, included in the pre-study report by Johansson et al. (2018). In light of this pre-study report, the specific research issues in Section 1.2 were formulated and then addressed in the appended research papers (A-E).

In the appended papers, the characterization of the LRC and model verification was based on the data presented in Johansson (2003), Mansson et al. (2006), and Glamheden and Curtis (2006). The geological conditions are of hard-jointed rock mass and the design specifications resemble the ones of the large-scale LRC constructed in Skallen.

For the numerical modeling, finite element (FE) analysis was used since it is a robust approach capable of including the different LRC components and complex boundary conditions. The commercial software package Abaqus v2020 (Dassault Systèmes Simulia Corp., 2019) was used for the FE modeling, simulation and analysis. Python scripting was used to build the FE models and automate sequential simulations and analyses of several inputs, needed for the reliability-based analysis.

In Paper A, the response of the rock mass to the LRC gas pressurization is studied. An analytical model was derived based on equations in the report by Johansson et al. (1995) and compared with FE models. Paper B used FE models to study the interaction between lining components and the influence of discrete rock joint on the lining behavior. Papers C and D reviewed the subset simulation and response surface method, respectively, for the reliability-based design of LRCs. Paper E used the directional adaptive response surface approach combined with FE modeling to perform reliability-based analyses for the LRC design.

1.4. Outline of thesis

This thesis comprises a summarizing essay and five appended research papers (A-E). The essay includes four main chapters for the theoretical background of the appended papers. In Chapter 2, the LRC modeling is presented. Chapter 3 gives the different structural responses of the LRC. Chapter 4 includes the modelling of uncertainties. In Chapter 5, the reliability-based analysis for the calculation of low probabilities of failure is presented. The appended papers are summarized in Chapter 6. In Chapter 7, the implication of the findings from the appended papers is discussed. Conclusions and suggestions for future research are presented in Chapter 8.

1.5. Limitations

This thesis focuses on the model development and implementation for reliability-based design of LRCs, in particular with respect to the rock mechanical aspects. Homogeneous rock mass properties are assumed. These models were mainly verified against the available field data from the LRC in Skallen, southwestern Sweden. For further model development and validation, a larger amount of field test data from full-scale LRCs are necessary.

In this thesis, the total number of cycles to fatigue failure of the steel lining is in the transition between high and low-cycle fatigue. Fatigue of the steel lining was modeled based on a strain-range–fatigue-life approach. In an actual LRC design scenario, fatigue tests on welded samples embedded in hydrogen solution would be needed. A fracture mechanics approach would be needed to model the low-cycle fatigue in the welded plates.

2. Modeling of the lined rock cavern

In this chapter, the LRC modeling of geometry, in-situ stresses, gas pressure and temperature, rock mass properties, and lining properties are presented. The calculation of gas temperature is used in Section 3.6, mainly to show that thermal strains are not critical for the LRC design.

2.1. Geometry

For the modeling of the LRC in this thesis, large-scale and small-scale geometries were used as shown in Figure 2.1. In Figure 2.1a, the 3D LRC geometry is shown, which included the LRC internal radius, r_{i}, the LRC height, h_{c}, the overburden height above the LRC, h_{ob}, and the lining/concrete layer thickness, t_{c}. The cupola at the upper part of the LRC is modeled spherical with height equal to r_{i}. At the lower part of the LRC, the invert has a height, h_{b}, which may not be spherical. For the case of $h_{\mathrm{b}} < r_{\mathrm{i}}$, a circular smoothing with radius, r_{b}, smaller than h_{b}, is used for the smaller curvature between the cylindrical and invert parts of the LRC.

In Figure 2.1b, the LRC horizontal cross-section at $0.5h_{\mathrm{c}}$ is shown and the small-scale geometry of Figure 2.1c is indicated. The small-scale geometry of the lining models a rock joint, concrete layer, reinforcement, and steel lining. The reinforcement is embedded in the concrete layer, and interface interactions are defined at the rock-block–concrete-layer contact and concrete-layer–steel-lining contact (sliding layer). The arc length width of this geometry is based on a considered rock joint spacing, s_{j}. The reinforcement has diameter d_{r} and is placed at distance t_{r} from the steel lining of thickness t_{s}. The rebar spacing in the reinforcement, s_{r}, is considered as an equivalent cross-section area equal to $0.25\pi d_{\mathrm{r}}^2/s_{\mathrm{r}}$.

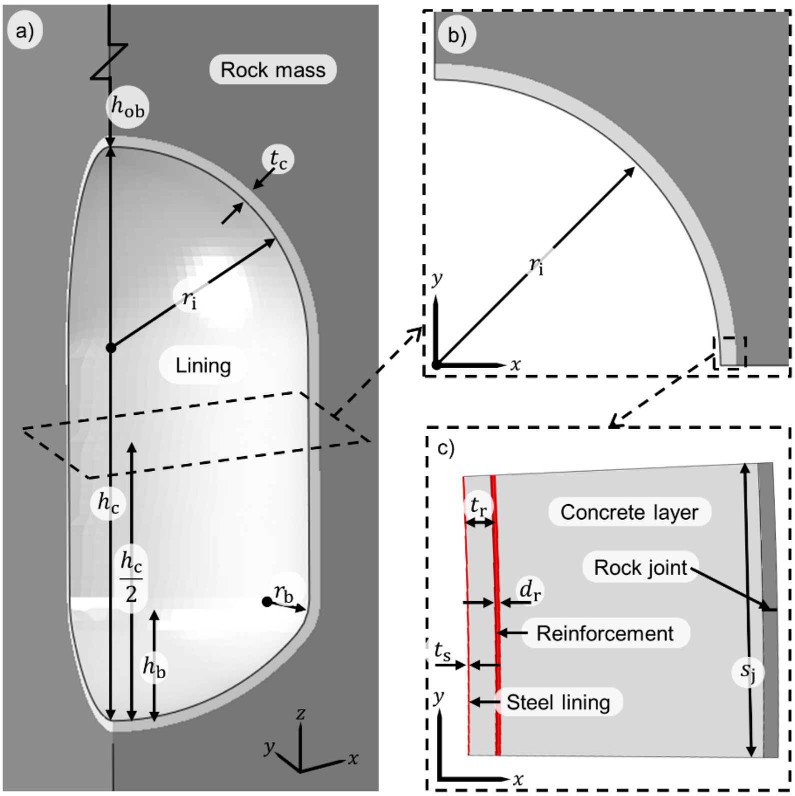

Figure 2.1. LRC a) 3D large-scale, b) 2D large-scale and c) 2D small-scale geometries used in this thesis. The 2D geometries are from the horizontal cross-section at the cavern mid-height.

The choice of geometry for the analyses in this thesis depends on the location where the wall tangential strain, $\varepsilon_{\theta\mathrm{w}}$, has the maximum value; which dictates the load effect on the steel lining. If the height is much larger than the diameter ($h_c \gg 2r_i$) and the invert is spherical ($h_b = r_b = r_i$), then the max($\varepsilon_{\theta\mathrm{w}}$) value locates at the cavern mid-height ($0.5h_c$) and a 2D plane-strain model (Figure 2.1b) can be used (Papers A, B and D). When the cupola is placed close to the invert, the LRC shape has an influence on the strains at the cavern mid-height and a 3D model (Figure 2.1a) is needed (Papers A, C and E). Concentrations of strains in the lining because of opening of rock joints and the interaction between individual lining components is studied using a 2D plane-strain model (Figure 2.1c) in Paper B. For the case of non-spherical invert ($h_\mathrm{b} < r_\mathrm{i}$), the $\max(\varepsilon_{\theta\mathrm{w}})$ value locates at the smoothed corner between the cylindrical and invert parts of the LRC and the 3D geometry (Figure 2.1a) is used (Paper E). The geometry of the LRC in Skallen, which is used as reference in this thesis, is presented in Johansson (2003), Glamheden and Curtis (2006) and Mansson et al. (2006). These LRC dimensions are r_i = 18 m, h_c = 51 m, h_ob = 115 m, t_c = 1 m, h_b = 9 m, t_r = 10 cm, d_r = 1.6 cm, t_s = 1.2 cm, and s_r = 15 cm. Geometrical effects on the magnitudes of $\varepsilon_{\theta\mathrm{w}}$ are presented in Section 3.4.

2.2. In-situ stresses

The in-situ stresses influence both the resistance of the LRC design and the load effect on the LRC design. In this thesis, the in-situ stresses are defined as

$$\sigma_\mathrm{v} = \rho_\mathrm{m} g z \tag{2.1}$$

$$\sigma_\mathrm{H} = k_\mathrm{H}\sigma_\mathrm{v} \tag{2.2}$$

$$\sigma_\mathrm{h} = k_\mathrm{h}\sigma_\mathrm{v} \tag{2.3}$$

where σ_v is the vertical in-situ stress calculated based on the overburden weight, ρ_m is the density of the rock mass, the gravitational acceleration is g = 9.81 m/s^2, σ_H and σ_h are the maximum and minimum horizontal in-situ stresses respectively, and k_H and k_h are horizontal in-situ stress ratios. Conditions of hard rock masses are considered for the characterization of σ_H and σ_h. Figure 2.2 shows the in-situ stress models for the Fennoscandian shield, Sweden and Skallen. Stephansson (1993) presented

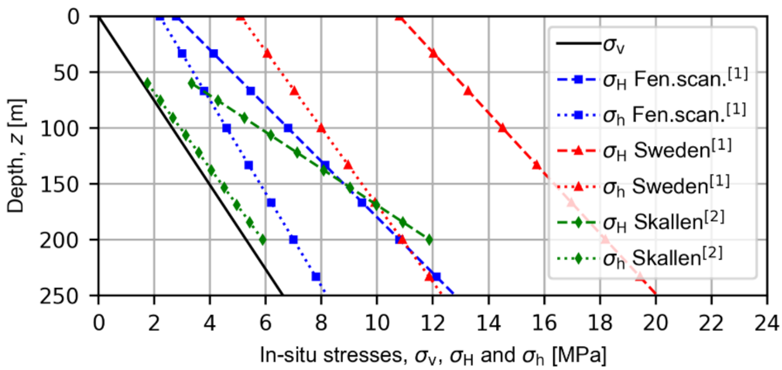

Figure 2.2. Models of σ_H and σ_h for the Fennoscandian shield, Sweden and Skallen. [1] Stephansson (1993); [2] Glamheden and Curtis (2006).

regression models of in-situ stress measurements with depth, z, from overcoring and hydraulic fracturing methods in the Fennoscandian rock stress database (FRSDB). In the Fennoscandian shield, the mean vertical stress is the minimum principal stress and has a minor magnitude difference with the minimum horizontal in-situ stress. The regression model for the average in-situ stress conditions in Sweden was also presented by Stephansson (1993) and has magnitudes of 1.5–2.5 times larger than σ_H and σ_h from the Fennoscandian shield. The in-situ stresses for the LRC in Skallen were modeled by Glamheden and Curtis (2006) and have a better agreement with the average in-situ stresses in the Fennoscandian shield. Other in-situ stress regression analyses in Sweden were presented by Glamheden et al. (2007) for the nuclear waste repository in Forsmark. The in-situ stresses from Skallen (Glamheden and Curtis, 2006) are considered for the reference LRC design, which give $k_H = 2.2$ and $k_h = 1.1$ calculated at the mid-height depth $z = 140.5$ m (Mansson et al., 2006). The influence of anisotropic in-situ stresses on the wall convergence during excavation of the rock cavern is visualized in Section 3.1.

2.3. Gas pressure and temperature

The filling and emptying of gas in the LRC results in volumetric expansion and contraction from variations in pressure and temperature of the gas. This thermodynamic behavior depends on the amount of stored gas and speed of storage cycles, influencing the mechanical and thermal strains of the LRC. A thermodynamic model for the average gas temperature in the LRC is presented here. In reality, the gas temperature is expected to be higher at the upper part of a large LRC; however, this level of detail is not included since it requires the use of more complex numerical models for computational fluid dynamics. The gas pressure, p_{i}, and gas temperature, T_{i}, inside a fixed LRC volume, V_{c}, vary during storage filling–emptying cycles. This variation takes place because of changes in the gas density, ρ_{g}, and the heat transfer with the surrounding rock mass (concrete layer behaves similarly to the rock mass). For each step of time, t, in this thermodynamic model, first the energy balance is solved for the gas inside the LRC and then another energy balance is solved for the rock mass at steps of radius from cavern center, r.

Bourgeois et al. (2015) proposed the energy balance for gas tanks of 0.1 m^3 with pressures up to 70 MPa in above ground conditions. Based on this approach, the energy balance for the gas in a full-scale LRC ($V_{\mathrm{c}} \approx 100\ 000$ m^3) is written as

$$\rho_{\mathrm{g}} V_{\mathrm{c}} c_{\mathrm{pg}} \frac{\partial T_{\mathrm{i}}}{\partial t} = V_{\mathrm{c}} \beta_{\mathrm{g}} T_{\mathrm{i}} \frac{\partial p_{\mathrm{i}}}{\partial t} + \frac{\bar{h}_{\mathrm{cg}} S_{\mathrm{c}}}{2} (T_{\mathrm{w}} - T_{\mathrm{i}}) + \frac{\partial \rho_{\mathrm{g}}}{\partial t} V_{\mathrm{c}} c_{\mathrm{pg}} (T_{\mathrm{n}} - T_{\mathrm{i}}) \tag{2.4}$$

where c_{pg} is the gas isobaric specific heat capacity, β_{g} is the gas isobaric thermal expansion, $\bar{h}_{\mathrm{cg}}$ is the surface average convective heat transfer coefficient between the cavern wall and the gas, S_{c} is the internal surface of the LRC, T_{w} is the temperature at the cavern wall, and T_{n} is the gas temperature at the inlet/outlet. Approximating a cylindrical shape for the LRC, the energy balance in the rock mass is obtained based on Bird et al. (2002) as

$$\rho_{\mathrm{m}} V_{\mathrm{m}} c_{\mathrm{pm}} \frac{\partial T_{\mathrm{m}}}{\partial t} = k_{\mathrm{pm}} S_{\mathrm{m}} \left(\frac{1}{r} \frac{\partial T_{\mathrm{m}}}{\partial r} + \frac{\partial^2 T_{\mathrm{m}}}{\partial r^2} \right) \tag{2.5}$$

where V_{m} is the volume of the rock mass within dr, c_{pm} is the specific heat capacity of the rock mass, T_{m} is the temperature in the rock mass, k_{pm} is the thermal conductivity of the rock mass and S_{m} is the surface area at r.

A gas state equation must be used for p_{i}. Olmos and Manousiouthakis (2013) showed that within the range of operational pressures of $0.1–100$ MPa and temperatures of $-70–225$°C the gas follows the Redlich–Kwong equation of state, which is given by

$$p_{\mathrm{i}} = \frac{R_{\mathrm{g}} T_{\mathrm{i}}}{v_{\mathrm{g}} - b_{\mathrm{g}}} - \frac{a_{\mathrm{g}}}{\sqrt{T_{\mathrm{i}}} v_{\mathrm{g}} \left(v_{\mathrm{g}} + b_{\mathrm{g}} \right)} \tag{2.6}$$

where the universal gas constant is $R_{\mathrm{g}} = 8.3145\ \mathrm{J/(K \cdot mol)}$, the molar volume is $v_{\mathrm{g}} = M_{\mathrm{g}} / \rho_{\mathrm{g}}$, M_{g} is the gas molar mass, and a_{g} and b_{g} are gas constants. The expressions for a_{g} and b_{g} are

$$a_{\mathrm{g}} = 0.4275 \frac{R_{\mathrm{g}}^2 T_{\mathrm{c}}^{2.5}}{p_{\mathrm{c}}} \tag{2.7}$$

and

$$b_{\mathrm{g}} = 0.0866 \frac{R_{\mathrm{g}} T_{\mathrm{c}}}{p_{\mathrm{c}}} \tag{2.8}$$

where T_{c} is the gas critical temperature and p_{c} is the gas critical pressure. The expression for β_{g} is derived by applying the reciprocal and cyclic permutation rules as

$$\beta_{\mathrm{g}} = \frac{1}{v_{\mathrm{g}}} \left(\frac{\partial v_{\mathrm{g}}}{\partial T_{\mathrm{i}}} \right)_{p_{\mathrm{i}}} = -\frac{1}{v_{\mathrm{g}}} \left(\frac{\partial v_{\mathrm{g}}}{\partial p_{\mathrm{i}}} \right)_{T_{\mathrm{i}}} \left(\frac{\partial p_{\mathrm{i}}}{\partial T_{\mathrm{i}}} \right)_{v_{\mathrm{g}}} = -\frac{1}{v_{\mathrm{g}}} \frac{\left(\partial p_{\mathrm{i}} / \partial T_{\mathrm{i}} \right)_{v_{\mathrm{g}}}}{\left(\partial p_{\mathrm{i}} / \partial v_{\mathrm{g}} \right)_{T_{\mathrm{i}}}} \tag{2.9}$$

where the partial derivatives of p_i are

$$\left(\frac{\partial p_\mathrm{i}}{\partial T_\mathrm{i}}\right)_{v_\mathrm{g}} = \frac{R_\mathrm{g}}{v_\mathrm{g} - b_\mathrm{g}} - \frac{a_\mathrm{g}}{2\sqrt[3]{T_\mathrm{i}}v_\mathrm{g}(v_\mathrm{g} + b_\mathrm{g})} \tag{2.10}$$

and

$$\left(\frac{\partial p_\mathrm{i}}{\partial v_\mathrm{g}}\right)_{T_\mathrm{i}} = -\frac{R_\mathrm{g}T_\mathrm{i}}{(v_\mathrm{g} - b_\mathrm{g})^2} + \frac{a_\mathrm{g}(2v_\mathrm{g} + b_\mathrm{g})}{\sqrt{T_\mathrm{i}}v_\mathrm{g}^2(v_\mathrm{g} + b_\mathrm{g})^2} \tag{2.11}$$

For $\bar{h}_\mathrm{cg}$, convective heat transfer was considered at the vertical walls of the LRC following the fundamentals of heat transfer (see textbook by Bergman et al., 2011). Due to the large size and slow filling–emptying rates of the LRC, free convective flow is assumed inside the storage and the correlation recommended by Churchill and Chu (1975) was used in the form

$$\bar{h}_\mathrm{cg} = \frac{k_\mathrm{pg}}{H_\mathrm{c}}\left\{0.825 + \frac{0.387Ra_{H_\mathrm{c}}^{0.167}}{\left[1 + \left(\frac{0.492}{Pr}\right)^{0.563}\right]^{0.296}}\right\}^2 \tag{2.12}$$

where k_pg is the thermal conductivity of the gas, H_c is the height of the LRC, Ra_{H_c} is the Rayleigh number based on the characteristic height H_c, and Pr is the Prandtl number. The expressions for Ra_{H_c} and Pr are

$$Ra_{H_\mathrm{c}} = \frac{g\rho_\mathrm{g}^2 c_\mathrm{pg}\beta_\mathrm{g}|T_\mathrm{w} - T_\mathrm{i}|H_\mathrm{c}^3}{\mu_\mathrm{g}k_\mathrm{pg}} \tag{2.13}$$

and

$$Pr = \frac{\mu_g c_{pg}}{k_{pg}} \tag{2.14}$$

where μ_g is the dynamic viscosity of the gas.

A prescribed change of ρ_g with time must be defined for this thermodynamic model with initial conditions for p_i, T_i and T_m. The partial derivatives are described using finite difference scheme with implicit time and discretization is performed with respect to r and t. The values of p_i and T_i at time $t + \Delta t$ are obtained numerically from the energy balance in the LRC. Then for the same time $t + \Delta t$, the energy balance in the rock mass is used to set a system of equations with solutions equal to the values of T_m along r. For this system of equations, the convective heat transfer term $(\bar{h}_{cg} S_c / 2)(T_i - T_w)$ is known and added only close to the boundary with the LRC wall.

Figure 2.3 shows the values of p_i and T_i changing with t, and T_m stabilized distribution along r/r_i, using monthly and weekly filling–emptying cycles. Since pressure and temperature field measurements are available only for natural gas storage in the Skallen LRC (Mansson et al., 2006), both methane, CH_4, and hydrogen gas, H_2, are considered for comparisons of p_i and T_i. Steps of $\Delta t = 0.25$ day and $\Delta r = 0.25$ m were used and average gas properties are available in the online database of the National Institute of Standards and Technology (NIST, 2022). A value of $\min(p_i) = 3$ MPa is initially set and the value of $\max(p_i) = 20$ MPa is considered by using the maximum gas densities of $\rho_g = 142$ kg/m^3 for CH_4 and 14 kg/m^3 for H_2. The calculated p_i and T_i shown in Figure 2.3a are within the field measurement magnitudes observed at the upper part of the LRC in Skallen (Mansson et al., 2006). Slightly smaller variations of p_i and T_i are observed for H_2 compared to CH_4, so the thermal strains in a hydrogen gas storage should be smaller than for a natural gas storage. The stabilized distributions of T_m are approximately the same regardless of the

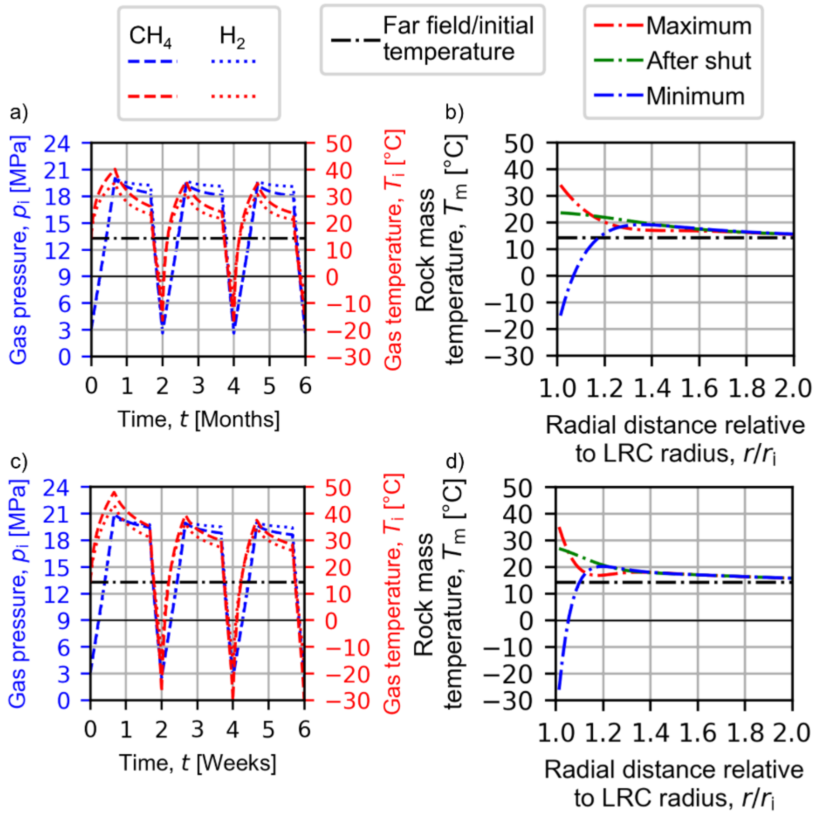

Figure 2.3. Thermodynamic model of the LRC gas filling–emptying for a) p_i and T_i changing with t and b) T_m distribution along distance into the rock mass r/r_i with monthly filling–emptying cycles, and c) p_i and T_i changing with t and d) T_m distribution along r/r_i with weekly filling–emptying cycles.

gas type, so only CH_4 is shown in Figure 2.3b and Figure 2.3d, for maximum gas pressure, after storage shut period, and minimum gas pressure. Most of the ΔT_m takes place within 2 m from the LRC wall. In Section 3.6, the temperatures calculated here are used to evaluate the influence of thermal strains on the LRC design.

2.4. Rock mass properties

The large-scale deformation and strength behaviors of the LRC are governed by the rock mass properties. Hoek and Brown (1980) proposed a rock mass failure criterion, which estimates rock mass properties by reducing the intact rock properties, obtained from laboratory experiments, based on geological observations in the field. Initially, the rock mass rating by Bieniawski (1989) was used as input, however, a more general rock mass classification was introduced later by Hoek et al. (1995) as the geological strength index (GSI). Hoek et al. (1995) presented a chart relating the condition and structure of the rock mass surface for the determination of a GSI between 0 and 100. The latest and most general version of this failure criterion was proposed by Hoek et al. (2002), which was used in this work for estimation of the mechanical properties of the rock mass.

In case the Young's modulus of the intact rock, E_i, is available, the Young's modulus of the rock mass, E_m, can be approximated from Hoek and Diederichs (2006) as

$$E_\mathrm{m} = E_\mathrm{i}\left[0.02 + \frac{1 - D/2}{1 + e^{(60+15D-GSI)/11}}\right] \tag{2.15}$$

where D is the degree of disturbance from the excavation, which varies from 0 for undisturbed to 1 for very disturbed rock masses. Alternatively, Hoek et al. (2002) proposed that

$$E_\mathrm{m} = \left(1 - \frac{D}{2}\right)\sqrt{\frac{f_\mathrm{ci}}{100}}\,10^{(GSI-10)/40+9} \tag{2.16}$$

where f_ci is the compressive strength of the intact rock.

Based on Hoek et al. (2002), the tensile strength of the rock mass can be estimated as

$$f_{\mathrm{tm}} = -\frac{s f_{\mathrm{ci}}}{m_{\mathrm{b}}} \tag{2.17}$$

where s and m_{b} are constants for the reduction of the rock mass strength and are calculated as

$$s = e^{(GSI-100)/(9-3D)} \tag{2.18}$$

$$m_{\mathrm{b}} = m_{\mathrm{i}} e^{(GSI-100)/(28-14D)} \tag{2.19}$$

The constant m_{i} is obtained from laboratorial triaxial test on intact rock samples. In this work, the unconfined compressive strength of the rock mass, f_{cm}, is expressed in terms of the cohesion of the rock mass, c_{m}, and friction angle of the rock mass, ϕ_{m}, as

$$f_{\mathrm{cm}} = \frac{2c_{\mathrm{m}}\cos(\phi_{\mathrm{m}})}{1-\sin(\phi_{\mathrm{m}})} \tag{2.20}$$

where c_{m} and ϕ_{m} are determined by least squares fitting of the Hoek–Brown relationship to the Mohr–Coulomb relationship. This gives (Hoek et al., 2002)

$$c_{\mathrm{m}} = \frac{f_{\mathrm{ci}}\left[(1+2a)s + (1-a)m_{\mathrm{b}}\frac{\sigma_{3\mathrm{max}}}{f_{\mathrm{ci}}}\right]\left(s+m_{\mathrm{b}}\frac{\sigma_{3\mathrm{max}}}{f_{\mathrm{ci}}}\right)^{a-1}}{(1+a)(2+a)\sqrt{1+\frac{6am_{\mathrm{b}}\left(s+m_{\mathrm{b}}\frac{\sigma_{3\mathrm{max}}}{f_{\mathrm{ci}}}\right)^{a-1}}{(1+a)(2+a)}}} \tag{2.21}$$

$$\phi_{\mathrm{m}} = \sin^{-1}\left[\frac{6am_{\mathrm{b}}\left(s+m_{\mathrm{b}}\frac{\sigma_{3\mathrm{max}}}{f_{\mathrm{ci}}}\right)^{a-1}}{2(1+a)(2+a)+6am_{\mathrm{b}}\left(s+m_{\mathrm{b}}\frac{\sigma_{3\mathrm{max}}}{f_{\mathrm{ci}}}\right)^{a-1}}\right] \tag{2.22}$$

where a is a constant for the reduction of the rock mass strength calculated using

$$a = \frac{1}{2} + \frac{1}{6}\left(e^{-GSI/15} - e^{-20/3}\right) \tag{2.23}$$

and $\sigma_{3\max}$ is the upper limit of the confining stress for the relationship between the Hoek–Brown and Mohr–Coulomb criteria, which can be estimated by

$$\sigma_{3\max} = 0.47 f_{\mathrm{gm}} \left(\frac{f_{\mathrm{gm}}}{\sigma_{\mathrm{co}}}\right)^{-0.94} \tag{2.24}$$

where f_{gm} is the global rock mass strength given as

$$f_{\mathrm{gm}} = f_{\mathrm{ci}} \frac{[m_{\mathrm{b}} + 4s - a(m_{\mathrm{b}} - 8s)] \left(\frac{m_{\mathrm{b}}}{4} + s\right)^{a-1}}{2(1+a)(2+a)} \tag{2.25}$$

and σ_{co} is the confining pressure. For the modeled LRC, the value of σ_{co} was considered to be equal the average in-situ stress, $\sigma_{\mathrm{o}} = (\sigma_{\mathrm{v}} + \sigma_{\mathrm{H}} + \sigma_{\mathrm{h}})/3$, during excavation of the rock cavern and equal to the $\max(p_{\mathrm{i}})$ during gas pressurization of the LRC.

The dilation angle of the rock mass, ψ_{m}, was estimated from Alejano and Alonso (2005) as

$$\psi_{\mathrm{m}} = \frac{\phi_{\mathrm{m}}}{1 + \log_{10}(f_{\mathrm{ci}})} \log_{10}\left(\frac{f_{\mathrm{ci}}}{\sigma_{\mathrm{co}} + 0.1}\right) \tag{2.26}$$

Residual parameters for the post-peak behavior can be estimated, as suggested by Cai et al. (2007), using the Hoek–Brown criterion with $D = 0$ and a reduced GSI_{r} calculated by

$$GSI_{\mathrm{r}} = GSI e^{-0.0134 GSI} \tag{2.27}$$

Rock mass properties for different GSI and f_{ci} are shown in Figure 2.4, considering input parameters of $m_{\mathrm{i}} = 25$ for a granitic rock type, $\sigma_{\mathrm{o}} = (3.7 + 8.1 + 4.1)/3 = 5.3$ MPa, and $\max(p_{\mathrm{i}}) = 25$ MPa. The residual

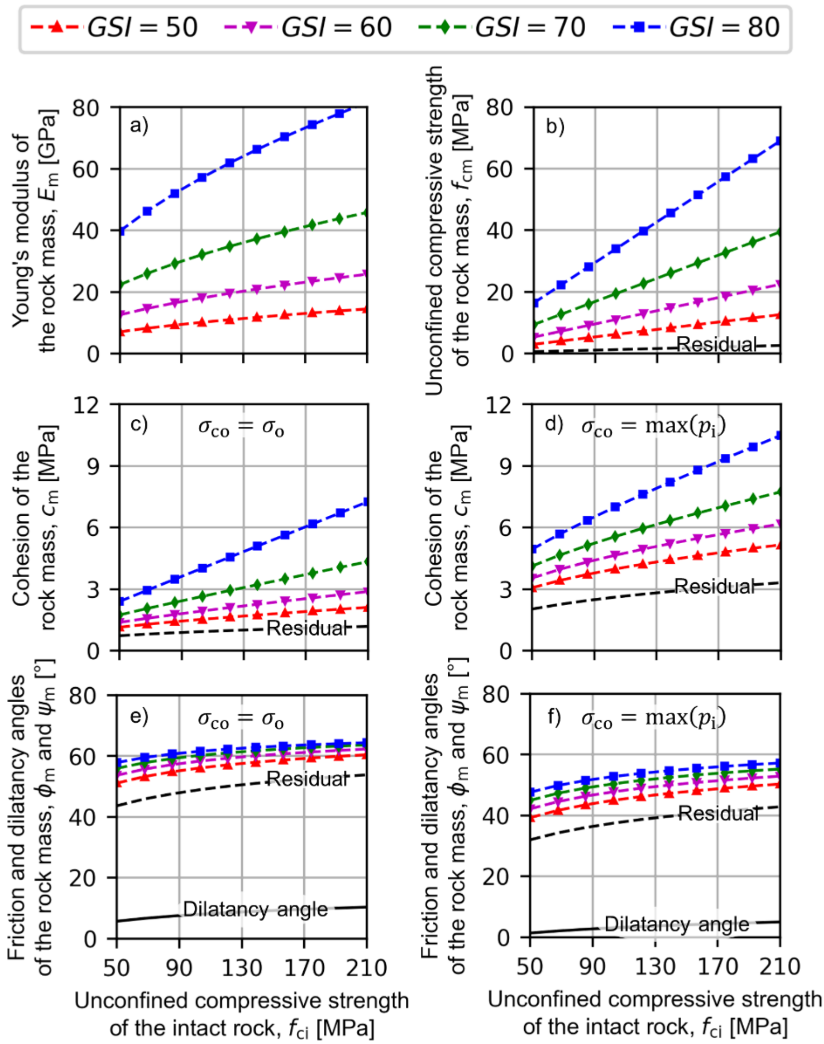

Figure 2.4. Rock mass properties a) E_{m}, b) f_{cm}, c) c_{m} with $\sigma_{\mathrm{co}} = \sigma_{\mathrm{o}}$, d) c_{m} with $\sigma_{\mathrm{co}} = \max(p_{\mathrm{i}})$, e) ϕ_{m} and ψ_{m} with $\sigma_{\mathrm{co}} = \sigma_{\mathrm{o}}$, and f) ϕ_{m} and ψ_{m} with $\sigma_{\mathrm{co}} = \max(p_{\mathrm{i}})$. Residual rock mass properties are indicated.

strength properties have similar magnitudes for different GSI values. The value of σ_{co} has an influence mainly on c_m, ϕ_m, and ψ_m. The rock mass properties influence on the calculations related to the rock cavern response is further presented in Chapter 3.

2.5. Lining properties

The lining properties that influence the mechanical behavior of the LRC concern the concrete material, steel material and contact interactions. Figure 2.5 shows material behaviors for these lining properties considering

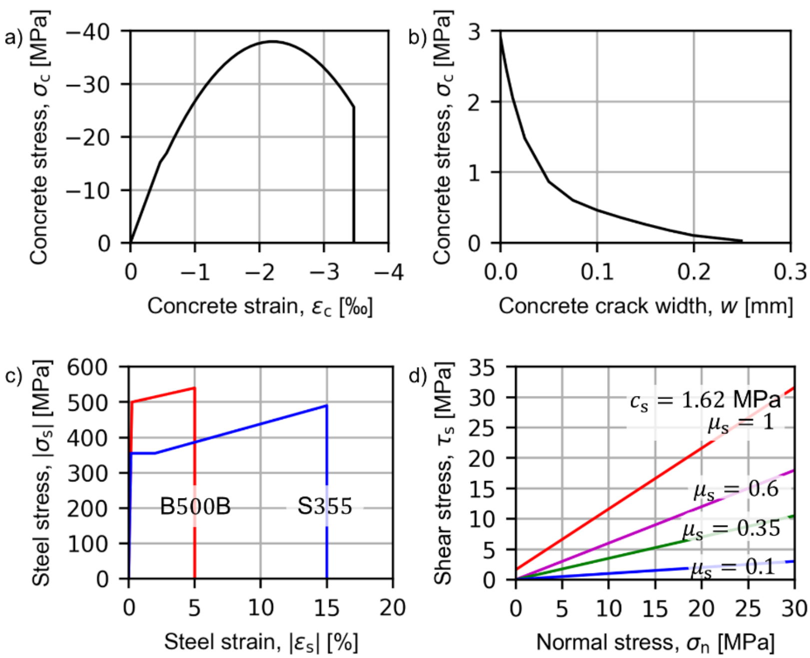

Figure 2.5. Lining component behaviors for a) concrete in compression, b) concrete in tension, c) steel, and d) interactions at the cohesive–frictional rock-block–concrete-layer contact and frictional concrete-layer–steel-lining contact.

previous LRC design in Skallen (Johansson, 2003). Compressive stresses and strains are identified with negative signs. The mathematical model used to calculate these curves are presented in the next subsections.

2.5.1. Concrete material

The concrete stress-strain, σ_c-ε_c, relationship in compression is shown in Figure 2.5a and is calculated by (CEN, 2005a)

$$\sigma_c = \left[\frac{1.05E_c \frac{\varepsilon_c}{f_{cc}} - \left(\frac{\varepsilon_c}{\varepsilon_{cc}}\right)^2}{1 + \left(1.05E_c \frac{\varepsilon_{cc}}{f_{cc}} - 2\right)\frac{\varepsilon_c}{\varepsilon_{cc}}}\right] f_{cc} \tag{2.28}$$

where E_c is the Young's modulus of concrete, f_{cc} is the compressive strength of concrete at 28 days and ε_{cc} is the concrete strain at maximum stress. In compression, the behavior of the concrete is assumed to be elastic up to $0.4f_{cc}$.

For the tensile behavior in Figure 2.5b, the magnitude of σ_c is expressed in terms of the crack displacement, w. The reason is to avoid variation of the fracture energy with respect to the FE element size. The exponential crack-opening expression is given by (Cornelissen et al., 1986)

$$\sigma_c = \left\{\left[1 + \left(\frac{c_1 w}{w_c}\right)^3\right] e^{-c_2 w/w_c} - \frac{w}{w_c}(1 + c_1{}^3)e^{-c_2}\right\} f_{tc} \tag{2.29}$$

where c_1 and c_2 are material constants, w_c is the stress-free crack width and f_{tc} is the tensile strength of concrete. For normal density concrete, $c_1 = 3$ and $c_2 = 6.93$. The magnitude of w_c is calculated using

$$w_c = 5.14 \frac{G_f}{|f_{tc}|} \tag{2.30}$$

where G_f is the fracture energy and, following fib (2010), can be estimated with $G_f = 73(f_{cc}/10^6)^{0.18}$.

The guidelines presented by Malm (2016) for FE analysis of concrete structures were used in this work to model the concrete layer of the LRC. The research by Lubliner et al. (1989) and Lee and Fenves (1998) lead to the damaged plasticity model which is commonly used to model crack initiation and development in concrete structures. This model simulates a crack as a reduction in the FE element stiffness. The concrete class C30/37 (CEN, 2005a) was used for the concrete layer and the dilation angle of concrete, ψ_c, is suggested to be 30° (Malm, 2006). The values of eccentricity, biaxial failure ratio and shape of yield surface of 0.1, 1.16 and 0.67, respectively, were used (Dassault Systèmes Simulia Corp., 2019).

2.5.2. Steel material

Figure 2.5c shows the metal plasticity stress-strain, σ_s-ε_s, curves for the reinforcement and steel lining. The steel behaves elastically if $\varepsilon_s \leq f_{ys}/E_s$, where f_{ys} is the yield strength of the steel and E_s is the Young's modulus of the steel. Typically, $E_s \approx 200$ GPa for all steel types. The steel work curve for $\varepsilon_s > f_{ys}/E_s$ is given by

$$\sigma_s = f_{ys} + (f_{us} - f_{ys})\frac{\varepsilon_s - \varepsilon_{hs}}{\varepsilon_{us} - \varepsilon_{hs}} \tag{2.31}$$

where f_{us} is the ultimate strength of steel, ε_{hs} is the steel strain hardening initiation, ε_{us} is the steel strain at ultimate failure. The values of f_{ys} and f_{us} are specified for different steel types. The steel type B500B was used for the reinforcement and steel type S355 (CEN, 2005b) was used for the steel plates, respectively. For the steel strain limits, typical values for high-strength reinforcing steels are $\varepsilon_{hs} \approx 0\%$ and $\varepsilon_{us} \approx 5\%$ and more ductile steels, used in the steel lining, have $\varepsilon_{hs} \approx 2\%$ and $\varepsilon_{us} \approx 15\%$. Hydrogen embrittlement may have an influence on the steel properties, however, this effect is not considered here.

2.5.3. Contact interactions

Figure 2.5d shows the modeled contact interactions within the lining. Contact interactions were considered at the rock-blocks–concrete-layer interface and at the sliding layer, i.e. at the concrete-layer–steel-lining interface. The slip initiation at a frictional–cohesive contact is described by the Mohr–Coulomb criterion, as

$$\sigma_{\mathrm{n}} = \mu_{\mathrm{s}}\tau_{\mathrm{s}} + c_{\mathrm{s}} \tag{2.32}$$

Bjureland et al. (2019) provided field data showing that the adhesion of shotcrete to a rock surface is about 0.81 MPa. The Griffith criterion was used to estimate the interface cohesion as $c_{\mathrm{s}} = 2 \cdot 0.81 = 1.62$ MPa. Laboratory experiments by Krounis et al. (2016) gave an average value of $\mu_{\mathrm{s}} = 1.4$ for the bounded contact between rock and concrete. In this work, a slightly more conservative value of $\mu_{\mathrm{s}} = 1$ was assumed. For the sliding layer at the interface between the concrete layer and the steel lining, a frictional contact was modeled ($c_{\mathrm{s}} = 0$). This contact could have a coefficient of friction as low as $\mu_{\mathrm{s}} = 0.1$ if bitumen is used (Johansson, 2003) or as high as $\mu_{\mathrm{s}} = 0.6$ without any sliding interface (Baltay and Gjelsvik, 1990).

3. Structural response of the lined rock cavern

In this chapter, the structural responses of the excavation of the rock cavern, failure of the steel lining, uplifting of the overburden rock mass, tangential strains at the rock cavern wall, steel lining strain concentrations at concrete cracks, and thermal strains in the steel lining are presented. These responses depend on the LRC modeling presented in Chapter 2. For the LRC design in this thesis, the excavation of the rock cavern and the thermal strains in the steel lining are not critical as explained at their specific sections below.

3.1. Excavation of the rock cavern

During excavation of the rock cavern, falling of large rock blocks at the roof is prevented by systematic bolting and shotcrete is used to secure the walls. The diameter of the rock cavern is large, so the rock mass must withstand all the wall convergence from excavation.

Hoek and Brown (1980) and Brown et al. (1983) presented the ground response curve (GRC) to calculate the wall convergence of tunnels, assuming an average in-situ stress σ_{o}. The tunnel wall radial displacement, u_{i}, is given by

$$u_{\mathrm{i}} = \frac{1 + v_{\mathrm{m}}}{E_{\mathrm{m}}} \left(\frac{\sigma_{\mathrm{o}} - \sigma_{rs}}{f + 1} \right) \left[2 \left(\frac{r_{\mathrm{s}}}{r_{\mathrm{i}}} \right)^{f+1} + (f - 1) \right] r_{\mathrm{i}} \tag{3.1}$$

where σ_{rs} is the pressure at the boundary of shear-yielded rock mass, f is the ratio of plastic strain increments in the tangential and radial directions, and r_{s} is the radius of the shear-yielded rock mass. The pressure at the tunnel wall that corresponds to the tangential shear yielding limit of the rock mass is

$$f_{\mathrm{bs}} = \frac{2(\sigma_{\mathrm{o}} + a_{\mathrm{m}})}{1 + k_{\mathrm{m}}} - a_{\mathrm{m}} \tag{3.2}$$

where the attraction of the rock mass is $a_{\mathrm{m}} = c_{\mathrm{m}}/\tan(\phi_{\mathrm{m}})$, the lateral earth pressure coefficient of the rock mass is $k_{\mathrm{m}} = \tan^2(45 + \phi_{\mathrm{m}}/2)$. The expressions of f and r_{s} are

$$f = \frac{\tan(45 + \phi_{\mathrm{m}}/2)}{\tan(45 + \phi_{\mathrm{m}}/2 - \psi_{\mathrm{m}})} \tag{3.3}$$

and

$$r_{\mathrm{s}} = r_{\mathrm{i}} \left(\frac{\sigma_{r\mathrm{s}} + a_{\mathrm{mr}}}{p_{\mathrm{i}} + a_{\mathrm{mr}}} \right)^{1/(k_{\mathrm{mr}} - 1)} \tag{3.4}$$

and a_{mr} and k_{mr} are the residual values of a_{m} and k_{m}. If $p_{\mathrm{i}} \geq f_{\mathrm{bs}}$, then the rock mass behaves elastically and $\sigma_{r\mathrm{s}} = p_{\mathrm{i}}$. Otherwise, shear yielding of the rock mass takes place and $\sigma_{r\mathrm{s}} = f_{\mathrm{bs}}$.

The GRC is used as an estimation of the average convergence of the rock cavern wall when $h_{\mathrm{c}} \gg 2r_{\mathrm{i}}$. To account for the effect of anisotropic in-situ stresses and the shape of the rock cavern, a 3D FE model is needed. In Figure 3.1a, the value of u_{i} is calculated using a 3D FE model with the geological conditions of Skallen. The largest values of u_{i} are observed at the cavern mid-height in the direction of σ_{H}. The values of u_{i} at the mid-height horizontal cross-section of the rock cavern using the GRC and the 3D FE model are shown in Figure 3.1b. The GRC has a good agreement with the average u_{i} from the 3D FE model for large values of GSI and f_{ci}. However, the GRC is simplified and cannot predict the distribution of u_{i} at the cavern wall as in the 3D FE model. At the direction of maximum σ_{H}, the values of u_{i} are close to zero at a cavern wall distance of less than $2r_{\mathrm{i}}$. For the geological conditions and rock cavern shape in this thesis, resembling those in Skallen, the expected u_{i} after excavation is relatively small and thus not considered to be an issue for the LRC design.

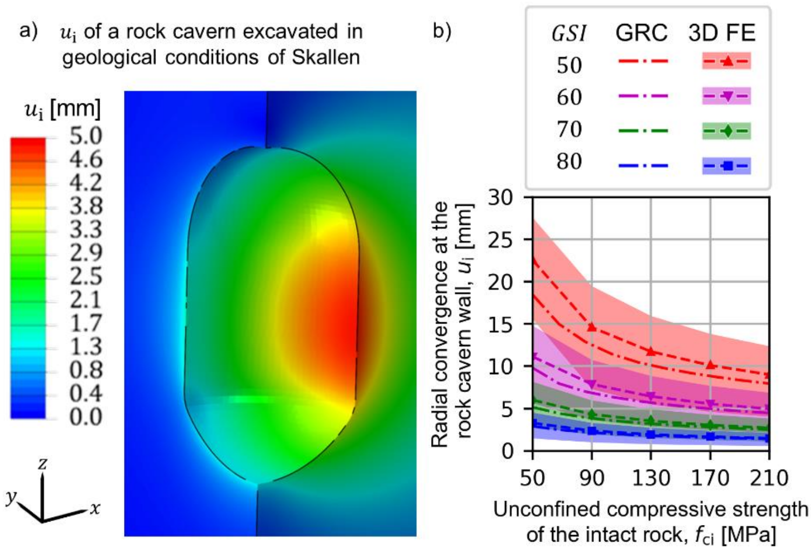

Figure 3.1. a) Values of u_i after the excavation of the rock cavern for the geological conditions of Skallen and b) comparison between maximum values from the GRC and the 3D FE model. Shaded areas in b) indicate the range of u_i values obtained from the 3D FE model.

3.2. Failure of the steel lining

The steel plates are welded together inside the rock cavern and concrete is cast between the rock mass and the steel lining. The LRC design is performed with the overarching aim of avoiding potential gas leakage from failure of the steel lining. Failure is expected to occur at a weakness point within the steel lining, e.g., a weld. Corrosion and hydrogen embrittlement of steel could reduce the life length of the LRC design; however, the specific effect on the steel properties is ongoing research and therefore not considered here.

Ultimate failure of the steel lining takes place only if excessively large strains occur at the LRC wall. The ultimate strain of the steel is represented by

$$\varepsilon_{\mathrm{us}} = \frac{f_{\mathrm{ys}}}{E_{\mathrm{s}}} + \sum \varepsilon_{\mathrm{ps}} \tag{3.5}$$

where $\sum \varepsilon_{\mathrm{ps}}$ is the cumulative plastic strain in the steel. If the maximum strain in the steel lining does not exceed the magnitude of $\varepsilon_{\mathrm{us}}$ during the first gas pressurization of the LRC; rupture of the steel lining can still occur if plastic strain takes place during the following gas pressurization cycles. Irreversible changes in the dimensions of the steel lining can result in irregularities at the LRC wall, leading to material failure. Therefore, no plastic strains in the steel lining may be allowed after the first gas pressurization, which is true for a maximum strain range of $\max(\Delta\varepsilon_{\mathrm{s}}) < 2f_{\mathrm{ys}}/E_{\mathrm{s}}$. Ultimate failure of the steel lining is considered in Paper B.

If ultimate failure of the steel lining does not occur, the critical failure mode is associated with the fatigue of the steel lining after several filling–emptying cycles. The fundamentals for the fatigue of materials is presented in Suresh (1998) and a strain-range–fatigue-life approach is assumed in this thesis. Estimations of the fatigue failure of a material relate the total number of cycles, n_{f}, given a constant strain range, $\Delta\varepsilon_{\mathrm{fs}}$. High-cycle fatigue is associated with elastic behavior of the material and a large number of cycles to failure ($n_{\mathrm{f}} > 10^4$), as shown by Basquin (1910). If the material yields at each cycle, then low-cycle fatigue will occur with failure for less cycles ($n_{\mathrm{f}} < 10^3$), following the relationship described by Coffin–Manson. The boundary limits for the transition between high-cycle and low-cycle fatigue are not well defined. The total strain range, $\Delta\varepsilon_{\mathrm{fs}}$, is achieved by combining these two formulas as shown by Coffin–Manson

$$\Delta\varepsilon_{\mathrm{fs}} = \frac{2f_{\mathrm{f}}'}{E_{\mathrm{s}}}(2n_{\mathrm{f}})^{b_{\mathrm{f}}} + 2\varepsilon_{\mathrm{f}}'(2n_{\mathrm{f}})^{c_{\mathrm{f}}} \tag{3.6}$$

where f_{f}' and $\varepsilon_{\mathrm{f}}'$ are the fatigue coefficients for strength and ductility, respectively, and b_{f} and c_{f} are the fatigue exponents for strength and ductility, respectively. These fatigue properties are obtained from fatigue experiments on cast metal in laboratory. In Paper C, reliability-based analysis was performed using the Coffin–Manson equation (Eq. (3.6)). Reductions in the $\Delta\varepsilon_{\mathrm{fs}}$ to account for the effect of welds were presented in Eurocode 3 for the design of steel structures (CEN, 2005b). The value of $\Delta\varepsilon_{\mathrm{fs}}$ for the LRC design case with $n_{\mathrm{f}} \leq 5 \cdot 10^6$ is estimated by

$$\Delta\varepsilon_{\mathrm{fs}} = \frac{f_{\mathrm{wc}}}{E_{\mathrm{s}}}\left(\frac{2 \cdot 10^6}{n_{\mathrm{f}}}\right)^{1/3} \tag{3.7}$$

where f_{wc} is the weld category. Butt-welding of the plates in the steel lining corresponds to a value of $f_{\mathrm{wc}} = 80$ MPa (CEN, 2005b) on the LRC design. The value of $\Delta\varepsilon_{\mathrm{fs}}$ considered in the Eurocode 3 is used in Papers A and E. Figure 3.2 shows the Coffin–Manson and Eurocode 3 approaches, which are used in this thesis.

3.3. Uplifting of the overburden rock mass

Uplifting the overlying rock mass takes place if the maximum gas pressure in the LRC, $\max(p_{\mathrm{i}})$, exceeds the pressure provided by the overburden rock

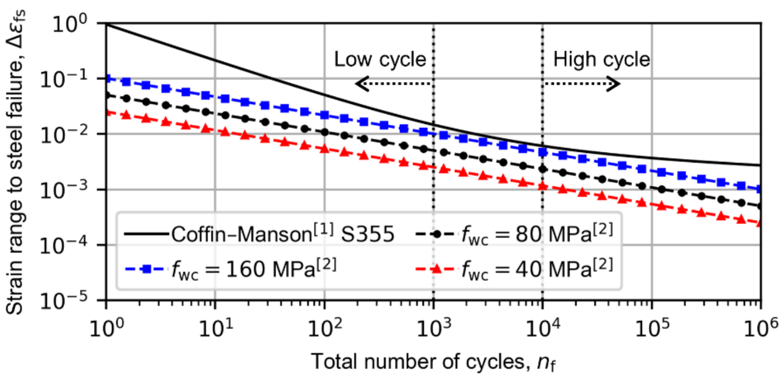

Figure 3.2. Values of $\Delta\varepsilon_{\mathrm{fs}}$ using the Coffin–Manson equation with steel S355 and the Eurocode 3 with $f_{\mathrm{wc}} = 160$ MPa (cast steel value), 80 MPa, and 40 MPa. [1] Suresh (1998), [2] CEN (2005b).

mass, as shown in the conceptual model in Figure 3.3a. In this case, excessively large strains would take place leading to ultimate failure of the steel lining. This failure mode is avoided by placing the cavern at sufficient depth.

The literature for the uplift pressure resistance is based on pull-out tests performed for circular flat anchors embedded in soil materials, e.g., Balla (1961), Vesic (1971), Vezole (2002). Such tests for rock materials are not available; however, larger uplift pressure resistances are expected compared to soil materials. The design principles for the minimum LRC depth is shown in Paper D. The uplift pressure resistance considering only the weight of the overburden rock mass, acting on a circular area just above the LRC, is

$$p_{\mathrm{uw}} = \frac{\rho_{\mathrm{m}} g h_{\mathrm{ob}}\{r_{\mathrm{i}}^2 + [r_{\mathrm{i}} + h_{\mathrm{ob}} \tan(\theta_{\mathrm{ob}})]^2 + r_{\mathrm{i}}[r_{\mathrm{i}} + h_{\mathrm{ob}} \tan(\theta_{\mathrm{ob}})]\}}{3r_{\mathrm{i}}^2} \tag{3.8}$$

where θ_{ob} is the inclination of the overburden failure shape, which is more conical at shallow depths (lower σ_{o}) and becomes more cylindrical with increasing depths (higher σ_{o}). An additional uplift pressure resistance

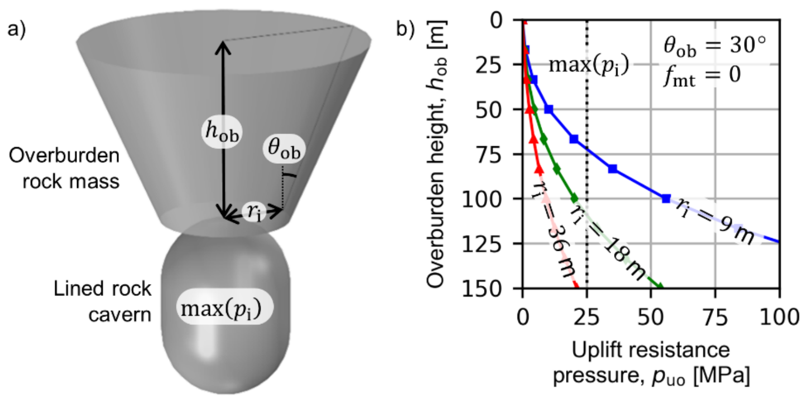

Figure 3.3. Uplift pressure resistance a) conceptual model, and b) calculation of p_{uo} as a function of h_{ob} for varying r_{i}. The dashed line for $\max(p_{\mathrm{i}})$ indicated the minimum value of p_{uo} in order to avoid uplifting of the overburden rock mass.

because of the tensile strength of the rock mass on top of the LRC can be included as

$$p_{\mathrm{ut}} = \frac{\{[r_{\mathrm{i}} + h_{\mathrm{ob}} \tan(\theta_{\mathrm{ob}})]^2 - r_{\mathrm{i}}^2\} f_{\mathrm{tm}}}{r_{\mathrm{i}}^2} \tag{3.9}$$

The minimum rock cover for the LRC design to avoid uplifting of the overburden rock mass is the value of h_{ob} that satisfies

$$p_{\mathrm{uo}} = p_{\mathrm{uw}} + p_{\mathrm{ut}} \tag{3.10}$$

In Figure 3.3b, p_{uo} is calculated as a function of h_{ob} for different values of r_{i}. Increasing values of r_{i} result in smaller p_{uo}. Failure of the LRC design because of uplifting of the overburden rock mass is avoided basically by setting a larger h_{ob}.

Alternatively, a 3D FE model could be used to evaluate the largest strains in the rock cavern wall as a function of the cavern depth in order to specify the minimum rock cover. Johansson (2003) presented the concept of a non-robust zone where the failure modes associated with the rock mass uplifting would take place. Below the depth of the non-robust zone, the decrease of lining strains with depth becomes small and close to linear. The non-robust zone approach is used in Paper A.

3.4. Tangential strains at the rock cavern wall

Johansson et al. (1995) presented equations for the rock mass response to the internal gas pressure, at the mid-height horizontal cross-section of the cavern. The full derivations of this model were presented in detail and updated to a more concise formulation in Paper A, which are summarized here. In Papers A and C, this analytical model is used. These derivations follow a similar framework as that of the GRC (Hoek and Brown, 1980, Brown et al., 1983); however, the direction of the deformation is into the rock mass because of the internal gas pressure. The conceptual model is shown in Figure 3.4, considering the rock cavern horizontal cross-section. This analytical model considers two possible yielding paths including elastic, tensile and shear deformations of the rock mass.

The average strains in the steel lining follow the tangential strains at the rock cavern wall, $\varepsilon_{\theta\mathrm{w}}$, which in turn are caused by internal gas pressurization. The expression for $\varepsilon_{\theta\mathrm{w}}$ is

$$\varepsilon_{\theta\mathrm{w}} = \left[\frac{k_\psi}{k_\psi + 1}\left(\varepsilon_{r\mathrm{ers}} + \frac{\varepsilon_{\theta\mathrm{ers}}}{k_\psi}\right) - \varepsilon_{\theta\mathrm{rs}}\right]\left(\frac{r_\mathrm{s}}{r_\mathrm{i}}\right)^{(k_\psi+1)/k_\psi} - \frac{k_\psi}{k_\psi + 1}\left(\varepsilon_{r\mathrm{ers}} + \frac{\varepsilon_{\theta\mathrm{ers}}}{k_\psi}\right) \tag{3.11}$$

where k_ψ is the ratio of plastic strain increments in the tangential and radial directions, similar to f, but derived based on the principal stresses as

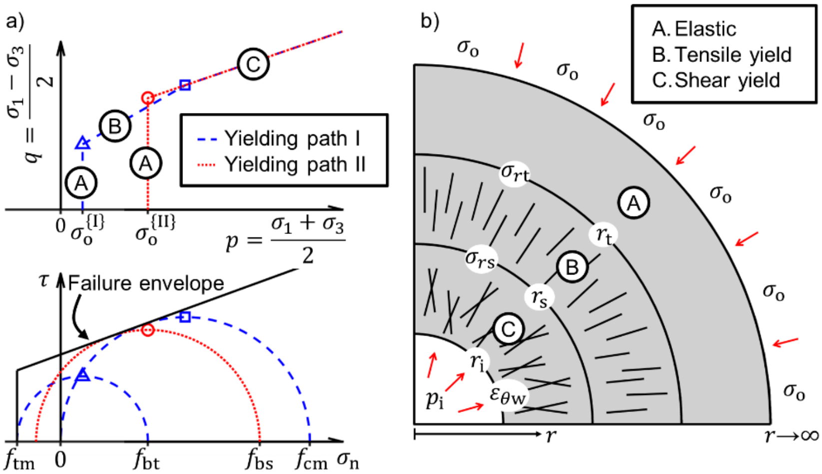

Figure 3.4. Conceptual model showing a) two possible stress paths and corresponding Mohr circles at yielding initiation, and b) development of rock mass responses for yielding path I. For yielding path II, tensile yield does not take place (figure from Paper A with minor modifications, CC BY-NC-ND 4.0 https://creativecommons.org/licenses/by-nc-nd/4.0/).

$$k_{\psi} = \tan^2\left(45 + \frac{\psi_\mathrm{m}}{2}\right) \tag{3.12}$$

The parameters $\varepsilon_{r\mathrm{ers}}$, $\varepsilon_{\theta\mathrm{ers}}$ and $\varepsilon_{\theta\mathrm{rs}}$ are the elastic radial strain, elastic tangential strain and total, i.e., elastic + plastic, tangential strain at the radius of the shear-yielded rock mass, r_s. These strains are expressed by

$$\varepsilon_{r\mathrm{ers}} = \frac{1+v_\mathrm{m}}{E_\mathrm{m}}\left[(1-v_\mathrm{m})\sigma_{rs} + v_\mathrm{m}\sigma_{rt} - \sigma_\mathrm{o} + \sigma_\mathrm{o}\left(\frac{r_\mathrm{i}}{r_\mathrm{s}}\right)^2\right] \tag{3.13}$$

$$\varepsilon_{\theta\mathrm{ers}} = -\frac{1+v_\mathrm{m}}{E_\mathrm{m}}\left\{[\sigma_{rt} - 2(1-v_\mathrm{m})\sigma_\mathrm{o}]\frac{r_\mathrm{t}}{r_\mathrm{s}} + (1-2v_\mathrm{m})\sigma_\mathrm{o} + \sigma_\mathrm{o}\left(\frac{r_\mathrm{i}}{r_\mathrm{s}}\right)^2\right\} \tag{3.14}$$

$$\varepsilon_{\theta\mathrm{rs}} = -\frac{1+v_\mathrm{m}}{E_\mathrm{m}}\left\{(v_\mathrm{m}-1)\sigma_{rs}\ln\left(\frac{r_\mathrm{s}}{r_\mathrm{t}}\right) + [(1+v_\mathrm{m})\sigma_{rt} - 2\sigma_\mathrm{o}]\frac{r_\mathrm{t}}{r_\mathrm{s}} - v_\mathrm{m}\sigma_{rt} + \sigma_\mathrm{o} + \sigma_\mathrm{o}\left(\frac{r_\mathrm{i}}{r_\mathrm{s}}\right)^2\right\} \tag{3.15}$$

where r_t is the radius of the tensile-yielded rock mass. The radii r_t and r_s are calculated by

$$r_\mathrm{t} = r_\mathrm{s}\frac{\sigma_{rs}}{\sigma_{rt}} \tag{3.16}$$

$$r_\mathrm{s} = r_\mathrm{i}\left(\frac{p_\mathrm{i}+a_\mathrm{mr}}{\sigma_{rs}+a_\mathrm{mr}}\right)^{k_\mathrm{mr}/(k_\mathrm{mr}-1)} \tag{3.17}$$

The radial stresses σ_{rt} and σ_{rs} are defined in Table 3.1 based on the magnitudes of p_i and strengths f_bt, f_bs, f_cm, and f_cmr expressed by

$$f_\mathrm{bt} = 2\sigma_\mathrm{o} - f_\mathrm{tm} \tag{3.18}$$

$$f_{\mathrm{bs}} = \frac{f_{\mathrm{cm}}+2k_{\mathrm{m}}\sigma_{\mathrm{o}}}{k_{\mathrm{m}}+1} \tag{3.19}$$

$$f_{\mathrm{cm}} = a_{\mathrm{m}}(k_{\mathrm{m}} - 1) \tag{3.20}$$

$$f_{\mathrm{cmr}} = a_{\mathrm{mr}}(k_{\mathrm{mr}} - 1) \tag{3.21}$$

Most of the irreversible deformations take place during the first gas pressurization of the LRC, so the tangential strain range at the rock cavern wall, $\Delta\varepsilon_{\theta\mathrm{w}}$, during filling–emptying cycles is elastic and expressed by

$$\Delta\varepsilon_{\theta\mathrm{w}} = \frac{1+v_{\mathrm{m}}}{E_{\mathrm{m}}}\Delta p_{\mathrm{i}} \tag{3.22}$$

The effect of anisotropic in-situ stresses and cavern shape can be considered using a 3D FE model, as shown in Papers A and E. Figure 3.5

Table 3.1. Definition of σ_{rt} and σ_{rs}.

Yielding sequence	Response
Yielding path I	Compressive elastic behavior
$f_{\mathrm{bt}} \leq f_{\mathrm{bs}}$	For $p_{\mathrm{i}} \leq f_{\mathrm{bt}}$, then $\sigma_{rt} = p_{\mathrm{i}}$
	For $p_{\mathrm{i}} \leq f_{\mathrm{cm}}$, then $\sigma_{rs} = p_{\mathrm{i}}$
	Tensile yield behavior
	For $p_{\mathrm{i}} > f_{\mathrm{bt}}$, then $\sigma_{rt} = 2\sigma_{\mathrm{o}}$
	Shear yield behavior
	For $p_{\mathrm{i}} > f_{\mathrm{cm}}$
	If $f_{\mathrm{cmr}} \geq 2\sigma_{\mathrm{o}}$, then $\sigma_{rs} = f_{\mathrm{cmr}}$
	If $f_{\mathrm{cmr}} < 2\sigma_{\mathrm{o}}$, then
	$\sigma_{rt} = \sigma_{rs} = (f_{\mathrm{cmr}} + 2k_{\mathrm{mr}}\sigma_{\mathrm{o}})/(k_{\mathrm{mr}} + 1)$
Yielding path II	Compressive elastic behavior
$f_{\mathrm{bs}} < f_{\mathrm{bt}}$	For $p_{\mathrm{i}} \leq f_{\mathrm{bs}}$, then $\sigma_{rt} = \sigma_{rs} = p_{\mathrm{i}}$
	Shear yield behavior
	For $p_{\mathrm{i}} > f_{\mathrm{bs}}$, then
	$\sigma_{rt} = \sigma_{rs} = (f_{\mathrm{cmr}} + 2k_{\mathrm{mr}}\sigma_{\mathrm{o}})/(k_{\mathrm{mr}} + 1)$

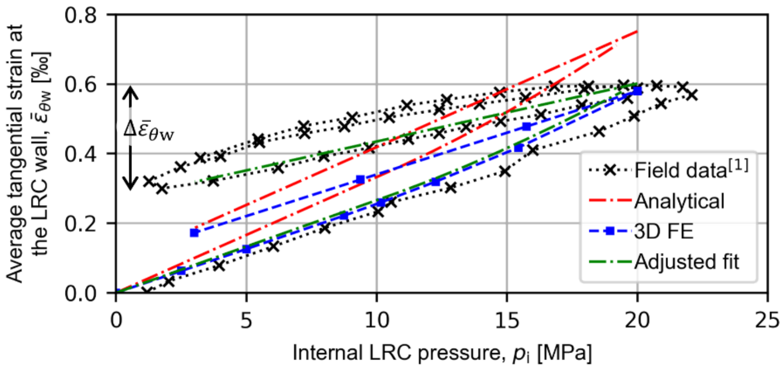

Figure 3.5. Values of $\bar{\varepsilon}_{\theta w}$ from field data, analytical model, 3D FE model, and adjusted analytical model. [1] Field data are retrieved from Mansson et al. (2006).

shows a comparison of the $\bar{\varepsilon}_{\theta w}$ (average) at the LRC mid-height obtained from the field data in Skallen (Mansson et al., 2006), the analytical model (Eqs. (3.11)–(3.22)), and a 3D FE model (Paper A). The result indicates that the analytical model overestimates $\bar{\varepsilon}_{\theta w}$ at $\max(p_i)$ and underestimates $\bar{\varepsilon}_{\theta w}$ at $\min(p_i)$. A larger value of $E_m = 45$ GPa in the first gas pressurization and $E_m = 72$ GPa for the cyclic behavior in the analytical model give a good fit with the field data. The 3D FE model has a good fit for the first gas pressurization; however, the value of range $\Delta\bar{\varepsilon}_{\theta w}$ for the following cycles is larger compared to the field data. A good fit of range $\Delta\bar{\varepsilon}_{\theta w}$ in the 3D FE model with the field data is obtained with a value of $E_m = 58$ GPa, which corresponds to a rock mass quality increase from $GSI = 70$ to $GSI = 75$.

For a 3D FE model with the geological conditions and shape of LRC in Skallen, the maximum $\varepsilon_{\theta w}$ takes place at the invert part of the LRC, as shown in Figure 3.6a for $p_i = \max(p_i) = 25$ MPa. Figure 3.6b shows the calculated maximum absolute strains $\max(\varepsilon_{\theta w})$ at the cylinder and invert parts of the LRC wall for different geological conditions. In Figure 3.6c, the corresponding maximum strain ranges $\max(\Delta\varepsilon_{\theta w})$ are shown considering a pressure range, Δp_i, from 3 MPa to 25 MPa. It can be observed that the invert corner gives larger strain magnitudes at the LRC wall than the cylinder part.

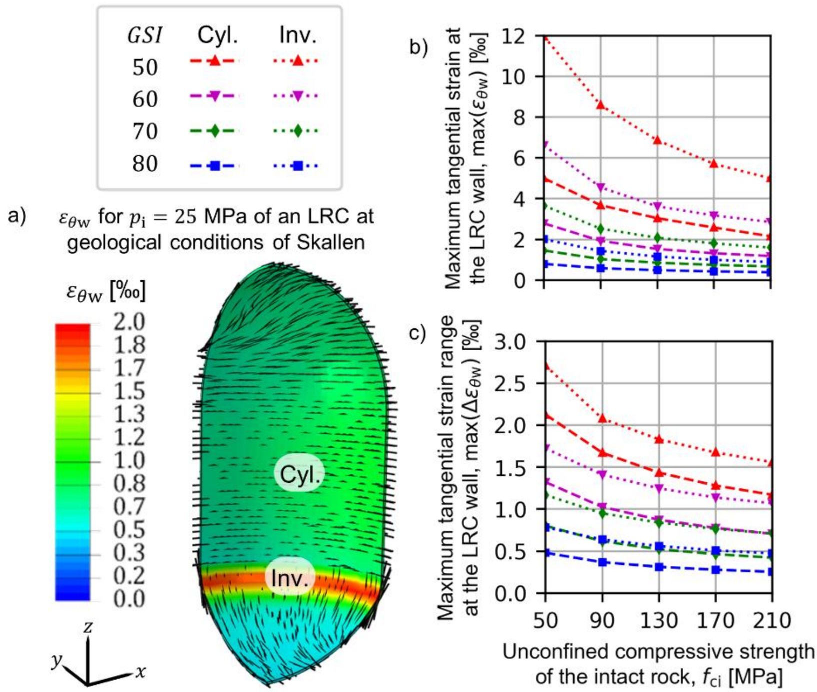

Figure 3.6. Calculation of $\varepsilon_{\theta w}$ using the 3D FE model for a) magnitudes and orientations at geological conditions of Skallen, and b) maximum absolute strains max($\varepsilon_{\theta w}$), and c) maximum strain ranges, max($\Delta\varepsilon_{\theta w}$), at the cylinder and invert parts of the LRC for different geological conditions.

3.5. Steel lining strain concentrations at concrete cracks

Tensile cracking of the concrete layer takes place even at low values of p_i and concentrate strains in the steel lining. The opening of rock joints at the cavern wall can induce concrete cracks with large widths, as shown in Figure 3.7a, further increasing the maximum strains in the steel lining and the risk for ultimate failure. Although larger strain magnitudes are observed in the steel lining compared to the rock cavern wall, the strain range in the steel lining follows the tangential strain range of the rock cavern wall.

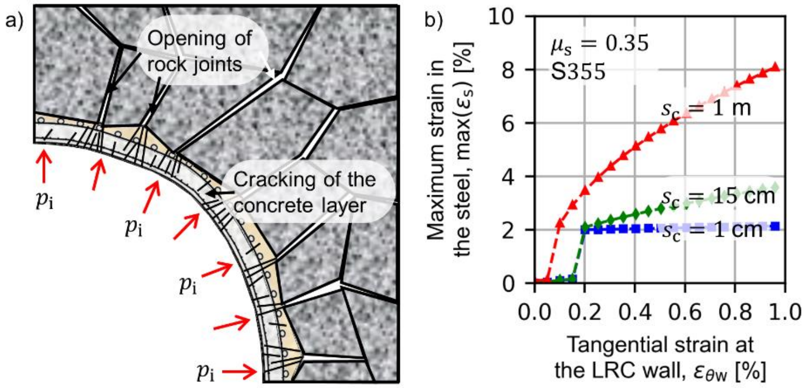

Figure 3.7. a) Conceptual model of the opening of rock joints and cracking of the concrete layer from gas pressurization of the LRC, and b) calculation of $\max(\varepsilon_s)$ as a function of $\varepsilon_{\theta w}$ for varying s_c.

Johansson (2003) presented equations for the calculation of strain distributions in the steel lining because of opening of concrete cracks. The appendix to Paper B presents the detailed derivations of this analytical model; a summary is provided in the following. The maximum stress in the steel lining is estimated using

$$\max(\sigma_s) = E_s \varepsilon_{\theta w} + \frac{\mu_s p_i}{t_s} \frac{s_c}{4} \tag{3.23}$$

where s_c is the average concrete crack spacing. If $\max(\sigma_s) \leq f_{ys}$, then the steel lining does not yield and the maximum strain in the steel lining, ε_s, is

$$\max(\varepsilon_s) = \frac{\max(\sigma_s)}{E_s} \tag{3.24}$$

However, if $\max(\sigma_s) > f_{ys}$, the steel lining yield, giving

$$\max(\varepsilon_s) = \varepsilon_{hs} + \frac{\mu_s p_i}{t_s} l_y \left(\frac{\varepsilon_{us} - \varepsilon_{hs}}{f_{us} - f_{ys}} \right) \tag{3.25}$$

where l_{y} is the yielding length in the steel lining. The expression for l_{y} has the form of the positive root of a second order equation as

$$l_{\mathrm{y}} = \frac{-b + \sqrt{b^2 - 4ac}}{2a} \tag{3.26}$$

where a, b and c are

$$a = \frac{\mu_{\mathrm{s}} p_{\mathrm{i}}}{t_{\mathrm{s}}} \left(\frac{\varepsilon_{\mathrm{us}} - \varepsilon_{\mathrm{hs}}}{f_{\mathrm{us}} - f_{\mathrm{ys}}} - \frac{1}{E_{\mathrm{s}}} \right) \tag{3.27}$$

$$b = 2 \left(\varepsilon_{\mathrm{hs}} - \frac{f_{\mathrm{ys}}}{E_{\mathrm{s}}} + \frac{\mu_{\mathrm{s}} p_{\mathrm{i}}}{t_{\mathrm{s}} E_{\mathrm{s}}} \frac{s_{\mathrm{c}}}{2} \right) \tag{3.28}$$

and

$$c = s_{\mathrm{c}} \left(\frac{f_{\mathrm{ys}}}{E_{\mathrm{s}}} - \varepsilon_{\theta \mathrm{w}} - \frac{\mu_{\mathrm{s}} p_{\mathrm{i}}}{t_{\mathrm{s}} E_{\mathrm{s}}} \frac{s_{\mathrm{c}}}{4} \right) \tag{3.29}$$

Using the analytical model of Eqs. (3.23)–(3.29) for a steel type S355, values of $\max(\varepsilon_{\mathrm{s}})$ are calculated as a function of $\varepsilon_{\theta \mathrm{w}}$, as shown in Figure 3.7b. Different value of s_{c} and a constant $\mu_{\mathrm{s}} = 0.35$ are considered. It can be observed that increasing values of s_{c} have a large influence on the strain concentrations in the steel lining. Large values of s_{c} can be the result of the opening of rock joints at the cavern wall, as illustrated in Figure 3.7a.

In Paper B, the main contribution was the development of a 2D FE model including cracking of the concrete layer because of the opening of a discrete rock joint at the cavern wall to calculate strain concentrations in the steel lining. This 2D FE model can capture the complex interaction between individual LRC components, and does not require the assumption of a concrete crack spacing, as needed for the analytical model (Eqs. (3.23)–(3.29)). Different concrete crack patterns develop depending on the interaction between LRC components. The concrete crack development is influenced by the FE mesh arrangement, which adds complexity to the analysis.

3.6. Thermal strains at the steel lining

Gas filling–emptying cycles cause the temperature inside the storage to vary, which induce thermal strains at the LRC wall. Most of the temperature variations in the rock mass (concrete layer behaves similarly) take place within a few meters of the LRC wall. The thermal strain, ε_{T}, in the rock mass surrounding the LRC is

$$\varepsilon_{\mathrm{T}} = \alpha_{\mathrm{s}} \Delta T_{\mathrm{m}} \tag{3.30}$$

where the coefficient of thermal expansion of solids is $\alpha_{\mathrm{s}} \approx 1.2 \cdot 10^{-5}/°\mathrm{C}$. For the weekly gas storage cycle using the thermodynamic model in Section 2.2, a maximum $\Delta T_{\mathrm{m}} = 22°\mathrm{C}$ and minimum $\Delta T_{\mathrm{m}} = -45°\mathrm{C}$ were obtained at the LRC wall, as shown in Figure 3.8a. These temperature ranges correspond to an LRC expansion of $\varepsilon_{\mathrm{T}} = 0.26‰$ during gas filling and LRC contraction of $\varepsilon_{\mathrm{T}} = -0.54‰$ during gas emptying. Figure 3.8b

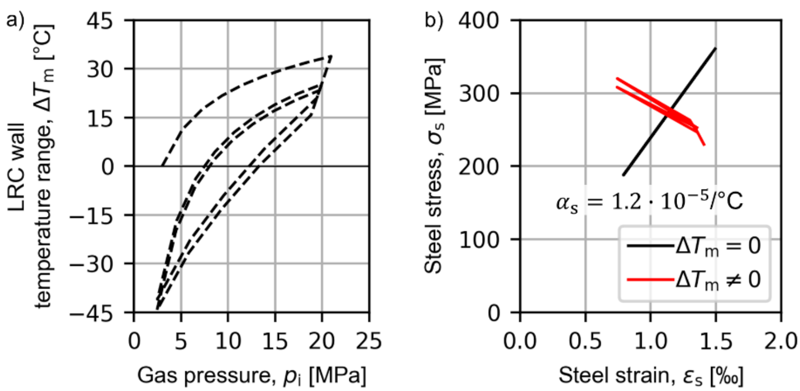

Figure 3.8. LRC behavior during filling–empting cycles for a) ΔT_{m} as a function of p_{i} and b) the effect of ΔT_{m} on σ_{s} and ε_{s}.

shows calculated steel stresses, σ_s, as function of steel strains, ε_s, from an FE model considering constant LRC temperature ($\Delta T_m = 0$) and varying LRC temperature ($\Delta T_m \neq 0$ in Figure 3.8a). When considering $\Delta T_m \neq 0$, not much difference is observed on ε_s compared to $\Delta T_m = 0$, only a slight reduction of 0.1‰ in the maximum steel strain. However, the values of σ_s rotate, having the maximum steel stress at $\min(p_i) = 3$ MPa and minimum steel stress at $\max(p_i) = 20$ MPa. Since the influence of gas temperature variations inside the LRC is small on the steel strain range and $\Delta T_m = 0$ gives slightly more conservative analysis, thermal strains are not considered for the LRC design in this thesis.

4. Modeling of uncertainties

This chapter presents how uncertain parameters are modeled in this thesis; however, the specific parameter distributions can be different for each geological site. Important uncertain parameters are presented for different performance functions in Section 5.2 (next chapter). Examples of parameter distributions are presented in Papers C, D and E.

4.1. Sources of uncertainty

A typical aspect of geotechnical engineering is the uncertainties associated with the description of the geological conditions. Modeling of these uncertainties is important to perform reliability-based analysis, which ensure safety requirements while avoiding overdesigning. Aleatory and epistemic uncertainties have been considered in geotechnical predictions (Lacasse and Nadim, 1996, Baecher and Christian, 2003, Ang and Tang, 2007).

Stochastic (aleatory) uncertainties are inherent of natural phenomena and cannot be reduced. For the case of epistemic (lack of knowledge) uncertainties, the variability can be reduced with more surveying and increase in knowledge. Types of uncertainties include

- Spatial: heterogeneity and anisotropy;
- Temporal: variations over time;
- Measurement: equipment, operator and limited data;

- Model: simplifications of the mathematical, physical and statistical descriptions; and

- Transformation: use of site-specific and empirical relationships.

The total uncertainty is often obtained from the combination of aleatory and epistemic uncertainties.

In this thesis, the considered uncertainties are mainly epistemic. The uncertainties and errors from measurement, model, and transformation should be accessed in practice based on sufficiently extensive surveying; however, these uncertainties and errors are not specifically addressed here because of insufficient field data. For a real design of an LRC, the initial design is typically based on a limited amount of data, and this design is updated as more data is acquired during the construction phase (see, e.g., Bjureland et al., 2017).

4.2. Description of uncertain properties

To perform a reliability-based analysis, the uncertain properties are modeled in the physical space with correlations and distributions using a matrix $\mathbf{X}$ with n_v different random variables at the rows and n_s samples at the columns. For the i^{th} random variable in $\mathbf{X} = [X_1, X_2, \dots, X_{n\mathrm{v}}]$, the sample variance is defined as

$$\sigma_i^2 = \frac{\sum_{n=1}^{n_\mathrm{s}} \left(x_{i,n} - \mu_i\right)^2}{n_\mathrm{s} - 1} \tag{4.1}$$

where σ_i is the standard deviation, $x_{i,n}$ is the n^{th} sample of the random variable X_i, and μ_i is the mean value. The value of μ_i is defined as

$$\mu_i = \frac{\sum_{n=1}^{n_\mathrm{s}} x_{i,n}}{n_\mathrm{s}} \tag{4.2}$$

and the coefficient of variation is expressed by

$$CV_i = \frac{\sigma_i}{\mu_i} \tag{4.3}$$

The correlation between samples of two random variables in **X** is defined by the correlation coefficient, as

$$\rho_{ij} = \frac{\sigma_{ij}}{\sigma_i \sigma_j} \tag{4.4}$$

where σ_{ij} is the covariance expressed as

$$\sigma_{ij} = \frac{\sum_{n=1}^{n_s}\left[(x_{i,n} - \mu_i)(x_{j,n} - \mu_j)\right]}{n_s - 1} \tag{4.5}$$

A large variety of uncertainties can be approximated by normally (Gaussian) distributed random variables with a probability density function described by

$$f_{Xi} = \frac{1}{\sigma_i \sqrt{2\pi}} \exp\left[-\frac{1}{2}\left(\frac{x_i - \mu_i}{\sigma_i}\right)^2\right] \tag{4.6}$$

However, geological properties can have large variability and negative values may be sampled if normal distributions are used. Lognormal distributions can be used to avoid sampling of unphysical values, as

$$f_{Xi} = \frac{1}{x_i \sqrt{\ln(1 + CV_i^2)}\sqrt{2\pi}} \exp\left\{-\frac{1}{2}\left[\frac{\ln(x_i) - \ln(\mu_i)}{\sqrt{\ln(1 + CV_i^2)}}\right]^2\right\} \tag{4.7}$$

For a random variable with small variability, the normal and lognormal distribution are similar, as shown in Figure 4.1a. At large variabilities, the lognormal distribution becomes more skewed compared to the normal distribution, as shown in Figure 4.1b, giving a smaller mode value.

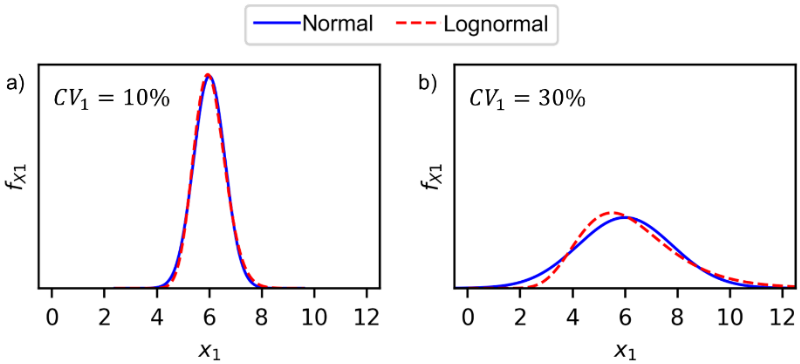

Figure 4.1. Normal and lognormal distributions for a) $CV_1 = 10\%$ and b) $CV_1 = 30\%$.

4.3. Correlation and distribution transformations

In reliability-based analysis, it is convenient to sample using independent random variables in the standard normal space, $\mathbf{U}$, since the desired samples matrix $\mathbf{X}$ can always be obtained using appropriate transformations for correlations and distributions (Rosenblatt, 1952). The standard normal space sampling is based on a probability density function f_{Ui}, which is the specific case of setting $x_i = u_i$, $\mu_i = 0$ and $\sigma_i = 1$ in Eq. (4.6). The Nataf transformation, as presented in Melchers and Beck (2018), is used in this thesis for the $\mathbf{U} \rightarrow \mathbf{X}$ transformation and is described in the following.

Correlated variables in the standard normal space, $\mathbf{U}_\mathrm{c}$, are obtained using

$$\mathbf{U}_\mathrm{c} = \mathbf{L}_\mathrm{c}\mathbf{U} \tag{4.8}$$

where $\mathbf{L}_\mathrm{c}$ is the lower triangular matrix of the correlation matrix. The matrix $\mathbf{L}_\mathrm{c}$ is found using Cholesky decomposition as

$$\mathbf{L}_{\mathrm{c}} = \begin{bmatrix} 1 & R_{12}\rho_{12} & \cdots & R_{1j}\rho_{1j} \\ R_{12}\rho_{12} & 1 & \cdots & R_{2j}\rho_{2j} \\ \vdots & \vdots & \ddots & \vdots \\ R_{1j}\rho_{1j} & R_{2j}\rho_{2j} & \cdots & 1 \end{bmatrix} \mathbf{L}_{\mathrm{c}}^{-T} \tag{4.9}$$

where R_{ij} are distribution correction factors (Melchers and Beck, 2018) between two random variables in $\mathbf{X}$. For normal–normal correlations, $R_{ij} = 1$ is used. If normal–lognormal correlations are considered, then

$$R_{ij} = \frac{CV_i}{\sqrt{\ln(1 + CV_i^2)}} \tag{4.10}$$

where i here is the index for the normally distributed random variable. For the case of lognormal–lognormal correlations, R_{ij} becomes

$$R_{ij} = \frac{\ln\left(1 + \rho_{ij} CV_i CV_j\right)}{\rho_{ij}\sqrt{\ln(1 + CV_i^2)}\sqrt{\ln\left(1 + CV_j^2\right)}} \tag{4.11}$$

Samples from each individual random variable u_{ci} in $\mathbf{U}_{\mathrm{c}}$ are then transformed to specific distributions. Normally distributed variables are described by

$$x_i = \mu_i + u_{ci}\sigma_i \tag{4.12}$$

while lognormally distributed variables are

$$x_i = \exp\left[\ln(\mu_i) + u_{ci}\sqrt{\ln(1 + CV_i^2)}\right] \tag{4.13}$$

Figure 4.2 shows the $\mathbf{U} \rightarrow \mathbf{U}_{\mathrm{c}} \rightarrow \mathbf{X}$ transformation, using two inversely correlated random variable with one normally distributed and another lognormally distributed.

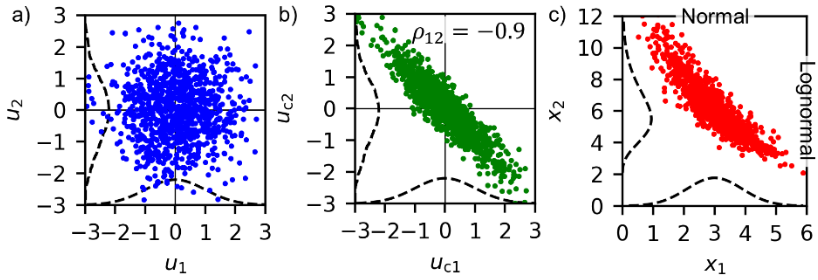

Figure 4.2. Random variable transformation from a) $\mathbf{U}$ in the independent standard normal space, to b) $\mathbf{U}_c$ in the correlated standard normal space, and to c) $\mathbf{X}$ in the correlated physical space.

4.4. Spatial variability

The influence of spatial variability on the LRC reliability, if any, is larger in the vertical direction because of the cavern excavation direction. The rock mass spatial variability of a i^{th} random variable can be estimated by calculating the autocorrelation vector, $\boldsymbol{\rho}_i$, with respect to the distance between two points in one direction. This can be described as (Baecher and Christian, 2003)

$$\boldsymbol{\rho}_i = \frac{\boldsymbol{\sigma}_{ir}}{\sigma_i^2} \tag{4.14}$$

where $\boldsymbol{\sigma}_{ir}$ is a vector of covariances for pairs of samples x_i and x_{ir} which are separated by a specified lag distance r. For each value of r, one value σ_{ir} is calculated using the expression given by (e.g. De Groot and Baecher, 1993)

$$\sigma_{ir} = \frac{\sum_{n=1}^{n_s}\left[\left(x_{i,n} - \mu_{ir}\right)\left(x_{ir,n} - \mu_{ir}\right)\right]}{n_r} \tag{4.15}$$

where μ_{ir} is a mean value defined based on the trend of $\mathbf{x}_i$, and n_r is the number of x_i–x_{ir} pairs. The terms $(x_{i,n} - \mu_{ir})$ and $(x_{ir,n} - \mu_{ir})$ correspond to natural inherent variabilities (residuals) of geological properties. For discrete field data, a lag interval $r + \Delta r$ is considered. If the lag distance is small ($r \approx 0$ m), high autocorrelation ($\rho_i \approx 1$) is expected. The scale of fluctuation, θ_i, is defined as the lag distance where the autocorrelation approaches zero.

If the length of the mechanical system, for instance the LRC height h_c, is larger than θ_i, a variance reduction can be applied as

$$\sigma_{i\mathrm{vr}}^2 = \Gamma^2 \sigma_i^2 \tag{4.16}$$

where Γ^2 is the variance function, defined at $0 < \Gamma^2 \leq 1$, and expressed for the vertical direction as, e.g., (Vanmarcke, 1977)

$$\Gamma^2 = \frac{\theta_i}{h_\mathrm{c}} \tag{4.17}$$

For geological conditions of a hard rock mass, which is relevant for this thesis, field measurements of the rock mass quality changing with depth are available for Forsmark in Sweden (Glamheden et al., 2007), as shown in Figure 4.3a. It is assumed that the variation of f_ci with depth is similar

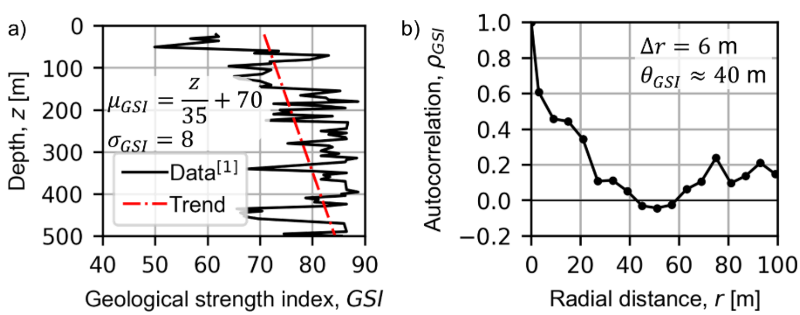

Figure 4.3. a) Variability of GSI with depth and b) calculation of autocorrelation. [1] Glamheden et al. (2007).

to the one of GSI presented here. The values of μ_{GSI} (linear trend) and σ_{GSI} are calculated and displayed in the figure. Figure 4.3b shows the calculated values of GSI autocorrelation $\boldsymbol{\rho}_{GSI}$ for different values of lag distance r using $\Delta r = 6$ m. The scale of fluctuation is $\theta_{GSI} \approx 40$ m, which is in the same order of magnitude of the LRC height of $h_c = 51$ m. Unless site-specific measurements are available, that show a considerably smaller scale of fluctuation, it is reasonable to take $\Gamma^2 = 1$. Therefore, variance reduction is not considered for the analyses in this thesis.

5. Reliability-based analysis

5.1. Structural reliability

A structural reliability analysis aims to obtain information regarding the capability of a design to fulfill its purpose within a period of time. The quantification of the structural performance, which accounts for the relevant uncertain variables, is made in terms of the probability of exceeding a certain limit state. A performance function, M_x, is used to evaluate this exceedance, often described by

$$M_x = R_x - S_x \tag{5.1}$$

where R_x is the resistance of the design, S_x is the load effect on the design, and the subscript x indicates description in the physical space. The limit state for the structural verification is identified as

$$M_x = 0 \tag{5.2}$$

which may refer to a serviceability or ultimate limit state.

The probability of exceeding the limit state is the probability of failure, expressed by the probability density of the failure region $M_x < 0$, as

$$P_\mathrm{f} = P(M_x \leq 0) = \int_{M_x \leq 0} f_\mathbf{X} d\mathbf{x} \tag{5.3}$$

where $f_\mathbf{X}$ is the joint probability density function of all random variables in $\mathbf{X}$. The structural reliability is simply the complement $1 - P_\mathrm{f}$. Likewise, a reliability index, β_{f}, can be used to express a design reliability. The values of P_{f} and β_{f} are related by

$$P_{\mathrm{f}} = P(M_u \leq -\beta_{\mathrm{f}}) = \int_{M_u \leq -\beta_{\mathrm{f}}} f_{\mathbf{U}} d\mathbf{u} \tag{5.4}$$

where the subscript $\mathbf{U}$ indicates description in the uncorrelated standard normal space. This relationship is simply expressed by $P_{\mathrm{f}} = \Phi(-\beta_{\mathrm{f}})$, where Φ is the cumulative density function in the standard normal space. Figure 5.1a indicates P_{f} and β_{f} within the distribution of M_u and Figure 5.1b shows the relationship between P_{f} and β_{f}.

The minimum standard normal distance from the mean values to the limit state gives the largest contribution for the design reliability calculation, and is used as an estimation of the β_{f} value, as

$$\beta_{\mathrm{f}} \approx \min|\mathbf{U}_{Mx=0}| \tag{5.5}$$

where $\mathbf{U}_{Mx=0}$ are all the coordinates of the limit state. The specific $\mathbf{U}_{Mx=0}$ coordinate that gives the minimum distance to the limit state is known as the design point, given by

$$\mathbf{U}_{\mathrm{d}} = -\boldsymbol{\alpha}_{\mathrm{d}}\beta_{\mathrm{f}} \tag{5.6}$$

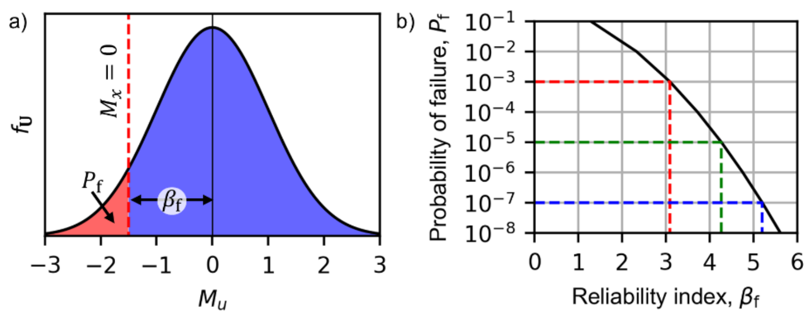

Figure 5.1. a) Representation of the distribution of M_u and $M_x = 0$, and b) relationship between P_{f} and β_{f}.

where $\boldsymbol{\alpha}_{\mathrm{d}}$ is a unit direction vector that indicates the weight (importance) of each random variable on the structural reliability.

If more than one performance function is of interest, the system reliability considering failure of the entire system at the weakest link is obtained by

$$P_{\mathrm{f}} = P\left(\bigcup M_x \leq 0\right) \tag{5.7}$$

which is the union of the exceedances of all considered limit states.

5.2. Acceptable probability of failure

An acceptable probability of failure of the structural design is represented by target values of probability of failure and reliability index, P_{ft} and β_{ft}. The Eurocode, for basis of structural design (CEN, 2002), suggests values of β_{ft} for ultimate failure of structures of different consequences. For LRCs, the following two consequence descriptions can be considered relevant:

- high consequence for loss of human life; or
- very high consequences in economy, society or environment.

For a reference period of 1 year or for the case of full correlation between annual failure events, the Eurocode suggests a target value of $\beta_{\mathrm{f}} \geq \beta_{\mathrm{ft}} = 5.2$ ($P_{\mathrm{f}} \leq P_{\mathrm{ft}} = 10^{-7}$). If failure events are not correlated, then a target value of $\beta_{\mathrm{f}} \geq \beta_{\mathrm{ft}} = 4.3$ ($P_{\mathrm{f}} \leq P_{\mathrm{ft}} = 10^{-5}$) is suggested for a reference period of 50 years of service life. For the LRC design in this thesis, the most important uncertainties are related to the geological conditions, which should not change over time. Therefore, it is assumed here that the failure events are fully correlated, so the higher target value of $\beta_{\mathrm{ft}} = 5.2$ is adopted in Paper E. Higher reliability requirements are not considered since such structural design needs individual considerations (CEN, 2002).

5.3. Performance functions

In this thesis, the LRC design concerns only ultimate limit states where rupturing of the steel lining implies leakage of the stored gas. The expressions for M_x used in this thesis are set based on the LRC structural responses presented in Chapter 3. The system reliability for the LRC design (Eq. (5.7)) includes the uplifting of the overburden rock mass, ultimate straining of the steel lining, and fatigue of the steel lining. However, system reliability is not addressed explicitly since fatigue of the steel lining was found to be the critical failure mode for conditions similar to the LRC in Skallen.

5.3.1. Uplifting of the overburden rock mass

The LRC performance function for the uplifting of the overburden rock mass depends on the uplifting pressure resistance, p_{uo}, and maximum gas pressure, $\max(p_{\mathrm{i}})$, and is defined as

$$M_x = p_{\mathrm{uo}} - \max(p_{\mathrm{i}}) \tag{5.8}$$

The main uncertainties related to the calculation of p_{uo} are the inclination of the overburden failure plane, θ_{ob}, and the tensile strength of the rock mass, f_{tm}. Paper D used this performance function for the reliability-based design with respect to the minimum LRC rock cover. Uplifting of the overburden rock mass should be unlikely if the cavern is placed at sufficient depth.

In practice, the value of θ_{ob} depends on the in-situ stresses and rock mass properties in the overburden. A 3D FE model can be used to account for these influences based on the non-robust zone concept (Johansson, 2003), which was used in Paper A. However, this approach is considerably more complex to implement in reliability-based analysis since each performance response requires the evaluation of tangential strain distributions at the LRC wall for different rock covers.

5.3.2. Ultimate straining of the steel lining

The performance function for the ultimate straining of the steel lining is based on the ultimate failure strain of the steel lining, $\varepsilon_{\mathrm{us}}$, and the maximum strain in the steel lining, $\max(\varepsilon_{\mathrm{s}})$, expressed as

$$M_x = \varepsilon_{\mathrm{us}} - \max(\varepsilon_{\mathrm{s}}) \tag{5.9}$$

The value of $\max(\varepsilon_{\mathrm{s}})$ depends on the geological conditions and lining properties. Main uncertainties are related to the geological strength index, GSI, unconfined compressive strength of the intact rock, f_{ci}, concrete crack spacing, s_{c}, and friction coefficient at the sliding layer, μ_{s}. Uncertainties in the maximum and minimum horizontal in-situ stresses, σ_{H} and σ_{h}, are also important if $\max(\varepsilon_{\mathrm{s}})$ locates at the cavern mid-height and is oriented horizontally. Based on laboratory experiments performed by Siddiqui and Abdullah (2005), hydrogen embrittlement may contribute with additional uncertainties in the steel properties associated with yielding and ultimate strengths, f_{ys} and f_{us}, as well as the hardening initiation and ultimate strains, $\varepsilon_{\mathrm{hs}}$ and $\varepsilon_{\mathrm{us}}$.

Ultimate straining of the steel lining is unlikely and not used in the reliability-based analysis in this thesis. The reason is that, based on Figure 3.7b and Paper B, a maximum tangential strain at the LRC wall of $\max(\varepsilon_{\theta\mathrm{w}}) = 0.6\%$ gave a value of $\max(\varepsilon_{\mathrm{s}}) \approx 2\text{–}3\%$ for both the analytical model (Eqs. (3.23)–(3.29)) and the 2D FE model. A value in the order of $\varepsilon_{\mathrm{us}} \approx 15\%$ is expected for the ductile steel used in the steel lining, which is sufficient to prevent failure because of ultimate straining. Even if an extreme scenario of $s_{\mathrm{c}} = 1\ \mathrm{m}$ with $\max(\varepsilon_{\theta\mathrm{w}}) = 1\%$ (Figure 3.6b) is considered, the resulting value of $\max(\varepsilon_{\mathrm{s}}) = 8\%$ (Figure 3.7b) would still not exceed the ultimate failure limit of the steel lining. In addition, rupture of the steel lining after the first gas pressurization is avoided for a maximum tangential strain range at the LRC wall of $\max(\Delta\varepsilon_{\theta\mathrm{w}}) < 3.55‰$ (steel type S355), which is not exceeded since all the considered cases in Figure 3.6c have values of $\max(\Delta\varepsilon_{\theta\mathrm{w}}) < 3‰$.

5.3.3. Fatigue of the steel lining

Fatigue failure of the steel lining depends on the strain range limit for fatigue failure of the steel lining, $\Delta\varepsilon_{\mathrm{fs}}$, and the actual value of $\max(\Delta\varepsilon_{\theta\mathrm{w}})$. The performance function is

$$M_x = \Delta\varepsilon_{\mathrm{fs}} - \max(\Delta\varepsilon_{\theta\mathrm{w}}) \tag{5.10}$$

The value of $\Delta\varepsilon_{\mathrm{fs}}$ (Eq. (3.7)) depends on the steel lining properties and $\max(\Delta\varepsilon_{\theta\mathrm{w}})$ depends on the geological conditions. A fixed total number of cycles n_{f} is considered here to represent the end of the service life. Paper C used this performance function for reliability-based analysis of LRCs with the analytical model by Johansson et al. (1995). The main uncertainties are the GSI, f_{ci}, and the weld category in the steel lining, f_{wc} (due to corrosion and hydrogen embrittlement). For $\max(\Delta\varepsilon_{\theta\mathrm{w}})$ oriented horizontally at the LRC wall, then σ_{H} and σ_{h} are also important uncertainties. Hydrogen embrittlement could have an effect on the value of f_{wc}, reducing $\Delta\varepsilon_{\mathrm{fs}}$. Paper E used a 3D FE model to calculate the value of $\max(\Delta\varepsilon_{\theta\mathrm{w}})$ including the influence of a corner at the LRC invert. Fatigue failure of the steel lining is considered the critical failure mode for the LRC design in this thesis.

5.4. Reliability calculation methods

In practice, the exact value of P_{f} and β_{f} is often not possible to obtain and calculation methods have been developed to approximate $\hat{P}_{\mathrm{f}}$ and $\hat{\beta}_{\mathrm{f}}$ numerically. These methods are divided into different levels based on the degree which uncertainties are accounted for. Melchers and Beck (2018) categorized calculation methods into

- Level I: application of partial factors to characteristic values of uncertainties;

- Level II: use of mean values, standard deviations and correlation coefficients with normally distributed uncertainties;

- Level III: consideration of joint distribution of all uncertainty;

- Level IV: consideration of consequences of failure for cost–benefit analyses.

The calculation of small probabilities of failure are influenced by the joint distribution of uncertain variables (El-Ramly et al., 2002). Therefore, level III methods are considered for the LRC design. “Conventional” reliability calculation methods are in the following considered to be those presented in textbooks, e.g. Melchers and Beck (2018). In this thesis, the following conventional methods are considered:

- Monte Carlo simulation (MCS)

- Directional simulation (DS)

- Response surface (RS) method

and the following “advanced” methods are considered:

- Subset simulation (SS)

- Adaptive directional importance sampling (ADIS) method.

These five methods are briefly explained in the next subsections.

A representation of each different sampling approach with number of samples used and variability of $\hat{\beta}_\mathrm{f}$ are shown in Figure 5.2. The RS method

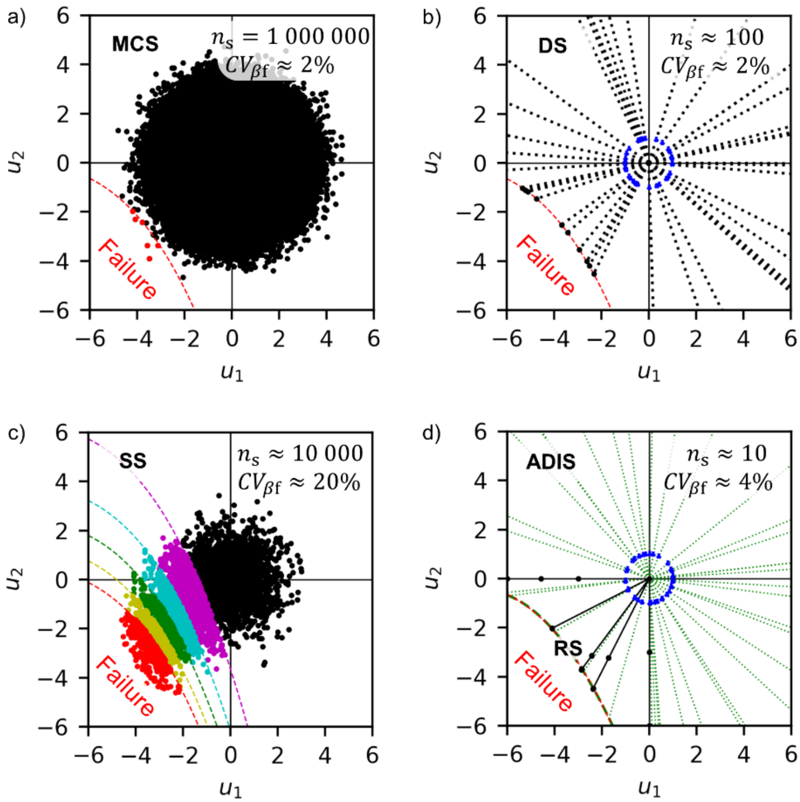

Figure 5.2. Sampling using a) MCS, b) DS, c) SS and d) ADIS with RS. Dots are samples and the red dashed lines are the limit states. The approximate values of n_s and $CV_{\beta f}$ are indicated for each approach.

is rather a surrogate modeling technique, which is considered within the ADIS method (Figure 5.2d). A synthetic performance function $M_x = (u_1 + 10)^3 + 100u_2$ is used for demonstration with standard normal variables and a target value of $\beta_{ft} = 4.48$. The variability of $\hat{\beta}_f$ is calculated in this thesis using

$$CV_{\beta f} = 1 + \frac{\Phi^{-1}(\hat{P}_f + \sigma_{Pf})}{\hat{\beta}_f} \tag{5.11}$$

5.4.1. Monte Carlo simulation

The MCS method (Figure 5.2a) is robust and easy to implement, but relies on a large number of random samples from the considered distributions and independent evaluations of M_x. These realizations cover a large number of combinations of input parameters to obtain the general distribution of M_x, as explained by Bernoulli's law of large numbers. The value of $\hat{P}_\mathrm{f}$ is calculated as

$$\hat{P}_\mathrm{f} = \frac{n_\mathrm{sf}}{n_\mathrm{s}} \tag{5.12}$$

where n_sf is the number of failed samples, i.e. that result in $M_x \leq 0$, and n_s is the total number of samples. The needed number of n_s to keep the efficiency of MCS is calculated as (Ang and Tang, 2007)

$$n_\mathrm{s} = \frac{1 - P_\mathrm{ft}}{P_\mathrm{ft} CV_{P\mathrm{f}}^2} \tag{5.13}$$

Setting $CV_{P\mathrm{f}} = 10\%$, the computation of $P_\mathrm{ft} = 10^{-7}$ (expected safety requirement for an LRC) would require $n_\mathrm{s} = 10^9$ (one billion samples), which becomes computationally difficult even if M_x is easy to evaluate.

Papers C and D used the MCS method for verification purposes. A large effort is put into the evaluation of M_x for samples in the whole stochastic domain (Figure 5.2a). For the calculation of small probabilities of failure, alternative methods that focus sampling close to the tail of the M_x distribution are able to reduce the required number of samples without sacrificing accuracy.

5.4.2. Directional simulation

The DS method (Figure 5.2b) uses polar coordinates to sample n_s random unit directions, $\mathbf{A}$, and integrates M_x along the radii of all sampled directions to find the corresponding distances to the limit state, β_i (Deak, 1980). Generating samples in standard normal space $\mathbf{U}$, the values of $\mathbf{A}$ can be obtained by

$$\mathbf{A} = \frac{\mathbf{U}}{|\mathbf{U}|} \tag{5.14}$$

The coordinates along the limit state are described by $\mathbf{U}_{Mx=0} = \mathbf{A}\boldsymbol{\beta}$, where $\boldsymbol{\beta}$ contains all the values of β_i. Each value of β_i is associated with a directional probability, as

$$P_{\mathrm{i}} = 1 - \chi^2_{n\mathrm{v}}(\beta_i^2) \tag{5.15}$$

where $\chi^2_{n\mathrm{v}}$ is the chi-square distribution function with degrees of freedom equal to the number of random variables, n_{v}. The unbiased value of $\hat{P}_{\mathrm{f}}$ is estimated using

$$\hat{P}_{\mathrm{f}} = \frac{\sum_{n=1}^{n_{\mathrm{s}}} P_{\mathrm{i},n}}{n_{\mathrm{s}}} \tag{5.16}$$

and the variance of $\hat{P}_{\mathrm{f}}$ is

$$\sigma^2_{P\mathrm{f}} = \frac{\sum_{n=1}^{n_{\mathrm{s}}} \left(P_{\mathrm{i},n} - \hat{P}_{\mathrm{f}}\right)^2}{n_{\mathrm{s}}(n_{\mathrm{s}} - 1)} \tag{5.17}$$

The DS method was used in Paper E as a part of the ADIS method. Integration of M_x at each direction may require a large number of evaluations to find the limit state. A line-search scheme based on polynomial regression models of low order can be used to find the limit state within two-to-three iterations. However, a large number of M_x evaluations are still needed since the value of β_i is searched in all directions. The DS method is however robust and efficient for the calculation of small probabilities of failure. Using a line search scheme, this method requires only a fraction of the required samples from MCS method for a similar accuracy (Figure 5.2b).

5.4.3. Response surface method

The RS method (Figure 5.2d) replaces a structural response described only by experiments or complex numerical models with an analytical polynomial model, G_x (Myers et al., 2009). This function G_x is easy to evaluate and can be implemented in any reliability calculation method for the estimation of $\hat{P}_\mathrm{f}$. A second order polynomial model of the performance responses $\mathbf{M}_x$ is constructed using regression analysis with respect to $\mathbf{U}$, by

$$G_x = b_0 + \sum\nolimits_{i=1}^{n_\mathrm{v}} b_i u_i + \sum\nolimits_{i=1}^{n_\mathrm{v}} b_{i+n_\mathrm{v}} u_i^2 \tag{5.18}$$

where $\mathbf{b} = [b_0, b_1, \dots, b_{2n\mathrm{v}}]$ are the least square coefficients estimated from regression analysis as

$$\mathbf{b} = (\mathbf{U}_\mathrm{r}^T \mathbf{U}_\mathrm{r})^{-1} \mathbf{U}_\mathrm{r}^T \mathbf{M}_x \tag{5.19}$$

where $\mathbf{U}_\mathrm{r}$ is the regression matrix which includes the samples $\mathbf{U}$ and depends on the order of the desired regression model. For a large number of random variables (high dimensions), a linear regression may be a more appropriate fit for the construction of G_x. The coefficient of determination, R^2, indicates that the regression model estimations fit well the expected responses for values close to 1, as

$$R^2 = \frac{\sum_{n=1}^{n_\mathrm{s}} \left(G_{x,n} - \mu_{Mx}\right)^2}{\sum_{n=1}^{n_\mathrm{s}} \left(M_{x,n} - \mu_{Mx}\right)^2} \tag{5.20}$$

The RS method was used in Papers D and E. In Figure 5.2d, a good fit of the limit state using the RS method is obtained in the ADIS method. Other surrogate modeling techniques involve kriging and backpropagation neural network (Jing et al., 2020).

5.4.4. Subset simulation

The SS method (Figure 5.2c) computes a small probability of failure by expressing it as the product of more frequent intermediate events (Au and Wang, 2014). The SS method initiates with an unconditional event using MCS with a subset number of samples n_c. Samples in the direction of failure region are defined as a percentage of the lowest M_x responses which correspond to a predefined subset conditional probability, P_c. These $P_\mathrm{c}n_\mathrm{c}$ samples are then taken as seeds in a Markov chain MCS for the generation of an intermediate event with n_c new samples. This procedure repeats generating new intermediate events in the direction of failure region until $M_x \leq 0$ is reached. After convergence of the SS method, $\hat{P}_\mathrm{f}$ is estimated by

$$\hat{P}_\mathrm{f} = P_\mathrm{c}^{n_\mathrm{l}-1} \frac{n_\mathrm{cf}}{n_\mathrm{c}} \tag{5.21}$$

where n_l is the number of intermediate events and n_cf is the number of failed samples at the last event. The total number of samples in the SS method is

$$n_\mathrm{s} = n_\mathrm{l} n_\mathrm{c} \tag{5.22}$$

Paper C investigated the SS method for LRC design. The SS method is more complex to implement than MCS; still, it requires a considerably large number of samples and has a large variability of $\hat{P}_\mathrm{f}$ (Figure 5.2c).

5.4.5. Adaptive directional importance sampling

The ADIS method (Figure 5.2d) combines DS and RS methods into a robust method, which is efficient in reducing the required number of samples while keeping an acceptable accuracy for the structural reliability calculation (Grooteman, 2011). Initial samples are taken along the axis of each random variable with DS method, evaluating M_x based on a line-search scheme and estimating the limit state location at $M_x = 0$ (Waarts, 2000). Based on these initial samples, regression analysis is used to create an analytical model G_x, as in the RS method, and importance directional sampling of M_x is performed only at the surrogate limit state $G_x = 0$. Based on additional evaluations of M_x, the surrogate model is updated and the structural reliability can be calculated using DS method on the surrogate G_x. The ADIS method converges when enough M_x evaluations are taken, leading to the convergence of $\hat{\beta}_{\mathrm{f}}$.

The detailed implementation of the ADIS method is presented in Paper E. In this thesis, this approach is the most efficient with respect to required number of samples and gives reasonably accurate estimations of the structural reliability (Figure 5.2d). This approach is therefore suitable for reliability-based analysis using computationally demanding FE simulations. The FE model needs to be robust within the stochastic sampling domain to avoid numerical convergence problems, e.g., because of geometry, mesh, boundary conditions, etc.

6. Summary of appended papers

This chapter summarizes the five appended papers. The reader seeking a complete understanding of the research results should here read the five papers instead, before reading the discussion and conclusions chapters.

6.1. Paper A

Damasceno, D. R., Spross, J., and Johansson, F., 2022. Rock mass response for lined rock caverns subjected to high internal gas pressure. Journal of Rock Mechanics and Geotechnical Engineering. In press. DOI: 10.1016/j.jrmge.2022.03.006.

Predicting the response of the rock mass is important to ensure that gas leakage due to rupture of the steel lining does not occur. This paper presents analytical and numerical models to estimate the maximum cavern wall tangential strain under a high internal pressure. The analytical model is derived in detail and FE models considering both 2D and 3D geometries are presented. These models are verified with field measurements from the LRC in Skallen. The analytical model is inexpensive to implement and gives good results for isotropic in-situ stress conditions and large cavern heights. For the case of anisotropic horizontal in-situ stresses, as the conditions in Skallen, the 3D FE model is the best approach.

6.2. Paper B

Damasceno, D. R., Spross, J., and Johansson, F., 2022. Strain concentrations in lined rock caverns subjected to internal gas pressure: effects of rock joints. Resubmitted to Journal of Rock Mechanics and Geotechnical Engineering.

Pressurizing the gas in the LRC storage causes joints in the rock mass to open, resulting in additional local straining of the lining. The structural interaction between the LRC components must be able to reduce the strain concentration in the sealing steel lining; however, this interaction is complex and difficult to model with analytical methods. In this paper, the strain concentration in LRCs from the opening of rock joints is studied using FE analyses, where the large- and small-scale behaviors of the LRC are coupled. The model includes concrete crack initiation and development with increasing gas pressure and rock joint width. The interaction between the jointed rock mass and the reinforced concrete, the sliding layer, and the steel lining is demonstrated. The results show that the rock mass quality and the spacing of the rock joints have the greatest influence on the strain distributions in the steel lining. The largest effect of rock joints on the maximum strains in the steel lining was observed for geological conditions of “good” quality rock masses.

6.3. Paper C

Damasceno, D. R., Spross, J., Johansson, F., and Johansson, J., 2019. Efficiency of subset simulation in the design of lined rock caverns for storage of hydrogen gas. Proceedings of the 13th International Conference on Applications of Statistics and Probability in Civil Engineering, Seoul, South Korea, ID 124.

High reliability is required for the storage of hydrogen gas and the computational time becomes unpractical for the evaluation of a complex structure such as the LRC. In this conference paper, the efficiency of SS regarding accuracy, precision and required number of samples is studied for the calculation of the design probability of failure against fatigue of the steel lining. By increasing the number of samples per level and increasing the conditional probability of failure, the precision increases as well as the total number of samples. The accuracy of the SS is checked with respect to MCS showing good agreement and with greater precision for fewer number of samples. A case study is performed for the geologic conditions of Sweden showing that the considered fatigue failure mode is unlikely for high stresses and good rock mass quality.

6.4. Paper D

> Damasceno, D. R., Spross, J., and Johansson, F., 2020. Reliability-based design methodology for lined rock cavern depth using the response surface method. Proceedings of the ISRM International Symposium - EUROCK 2020, Trondheim, Norway, ID 163.

The LRC storage must be placed at sufficient depth so that the overburden is able to resist the uplifting gas pressure from inside the cavern. Both the high reliability requirement and addressing the uncertainties related to the rock mass properties make it difficult to design for such structures. In this conference paper, a reliability-based design methodology for the LRC depth requirement, using the RS method, is presented. Geologic conditions of hard rock masses are considered. The analytical solution for the resistance to uplift takes into account both the tensile strength of the failure surface and the overburden weight pressure. The largest uncertainties are assumed to be related to the rock mass properties and correlations are considered. The results for cavern depth requirement are reasonable compared to previous experience. The efficiency of the RS method for the considered problem is observed both for required number of samples/computation time and accuracy, showing suitability to be used with more complex, difficult to evaluate, problems such as FE models.

6.5. Paper E

Damasceno, D. R., Spross, J., and Johansson, F., 2022. Reliability-based design tool for gas storage in lined rock caverns. Submitted to Georisk: Assessment and Management of Risk for Engineered Systems and Geohazards.

The LRC design needs to have a small probability of failure since the consequences of failure can be catastrophic. However, the current design practice for LRCs is deterministic, which limits the possibility to stringently address geotechnical uncertainties in the design. In this paper, a reliability-based design tool is presented for LRC gas storages. The ADIS method, which requires a relatively small number of samples, is used with a representative 3D FE model to evaluate small probabilities of failure. An illustrative example based on the LRC in Skallen, southwestern Sweden, demonstrates the implementation and applicability of the developed design tool. The considered uncertainties are related to geological conditions of hard rock masses and the steel lining. The results show that the reliability of this LRC design meets the expected safety requirements. Considering different geological conditions with correlations, at least "good" quality rock mass is needed for the LRC design. An additional sensitivity analysis is performed to study the potential influence of corrosion and hydrogen embrittlement on the reduction of the LRC design reliability.

7. Discussion

7.1. Development of lined rock cavern models

In this thesis, models to predict the LRC structural response to a high gas pressure were further developed to be used in reliability-based design. Based on the contributions for modeling development in this research, this section discusses the importance of the analytical model, the complex interaction between lining components, and the modeling aspects for the advanced reliability-based design.

7.1.1. Importance of the analytical model

In Paper A, the detailed derivation of an analytical model to calculate the tangential strains at the rock cavern wall was presented. Although limited to conditions of isotropic in-situ stress and idealized cavern geometry, this analytical model provides the ground for the theoretical and mathematical background of the LRC deformation behavior during gas storage. But this analytical model can also have a practical use for preliminary calculations of the LRC response. If average in-situ stresses are used as confining pressure, the tangential strains from the analytical model have a good agreement with the average tangential strains from a corresponding 2D FE model, as indicated by the calculations in Paper A. These calculations account for anisotropic in-situ stresses. For the LRC design, accounting for the effect of the 3D geometry at the cavern mid-height would, however, need a correction factor in a 2D analysis. The expected strain reduction at the cavern mid-height because of the 3D geometry effect, as observed in Paper A, could be adjusted by increasing the magnitude of the rock mass quality input in the analytical model. Also, a correction factor with respect to the in-situ stress ratio would be needed to convert the tangential strain magnitude from the average value to the maximum value. The effect of a smaller curvature localized at the cavern invert geometry has no significant influence on the strains at the cavern mid-height (Paper E), so a correction factor for this effect cannot be directly included to the present analytical model. This can be a problem for the design of LRC using the analytical model if conventional excavation techniques are used, as they may need to excavate a smaller curvature at the cavern invert. If the cavern invert can be excavated with a spherical shape, the maximum tangential strains at the rock cavern wall would instead be located at the cavern mid-height (Paper A), allowing the potential applicability of the analytical model for the LRC design.

7.1.2. Complex interaction between lining components

The complex interaction of LRC components was demonstrated using a 2D FE model in Paper B. One new aspect of this FE model was the coupling between large-scale and the small-scale deformation behaviors at the LRC mid-height. Another new aspect was the consideration of all main LRC components, including the jointed rock mass, concrete layer, reinforcement, sliding layer, and steel lining. Furthermore, the cracking of an initially intact concrete layer was considered, developing from the internal gas pressurization and opening of rock joints. The 2D model (Paper B) and 3D FE models (Papers A and E) agree with respect to negligible vertical strains at the cavern mid-height, so they are comparable for similar tangential strains at the rock cavern wall. Therefore, the small-scale 2D FE model in Paper B is representative at the mid-height of a real LRC geometry. This 2D FE model allowed the calculation of expected maximum tangential strains in the steel lining, considering the effect of all LRC components. The local contribution to the strains in the steel lining with respect to the opening of the rock joint and corresponding cracking of the concrete are also included in the 2D FE model. These results are important in order to be able to analyze the risk of steel lining rupture because of excessively large strains, i.e., ultimate failure.

7.1.3. Modeling aspects for the advanced reliability-based design

Paper E used a 3D FE model to calculate the tangential strain range at the LRC wall and perform advanced reliability-based analysis with respect to fatigue of the steel lining. This 3D FE model included the effects of cavern shape, gravitational loading, and installation of lining after excavation of the rock cavern. Gas filling and emptying of the storage were considered by applying a cyclic pressure to the internal walls of the lining. The largest tangential strains took place where the model had its smallest curvature. This 3D FE model gathered all of the most import aspects for the calculation of tangential strain ranges at the LRC wall. In order to minimize the occurrence of errors due to numerical convergence problems during the reliability-based analysis, the robustness of this 3D FE model was extensively tested with respect to material modeling, loading sequencing, geometry construction, and meshing arrangement. Similar tests were also performed to minimize the required computational time for the 3D FE simulations, and additional processing cores with parallel processing capabilities were used to further reduce the computation time. The 3D FE modeling aspects described here were essential to successfully enable advanced reliability-based analysis, and should be followed in practice for the reliability-based design of LRCs.

7.2. Reliability-based analysis

This section discusses the implementation of the reliability-based analysis considering both conventional and advanced reliability calculation methods as defined in Section 5.4.

7.2.1. Considerations for conventional methods

Conventional reliability-based analysis using, e.g., MCS is easier to implement and more broadly used in practice, instead of advanced reliability-based analysis such as the ADIS method. Although the best estimation of the LRC design reliability is given when a 3D FE model is used, an alternative conventional approach would be desirable if the accuracy of the design reliability estimation is not compromised.

Previous LRC design analyses by Johansson (2003) applied model correction factors to a simplified analytical model (Johansson et al., 1995) in order to use conventional reliability calculation methods. These model correction factors were based on a 3D FE model and aimed to include the effects of anisotropic in-situ stresses and cavern geometry on the analytical calculation of the maximum tangential strain at the LRC wall. However, based on the analytical model of Eq. (3.22) and on the 3D FE simulations from Paper E, shown in Figure 7.1, the relationship between these models is not linear and therefore the use of a single value for the correction factor is not appropriate. In addition, establishing a suitable model correction

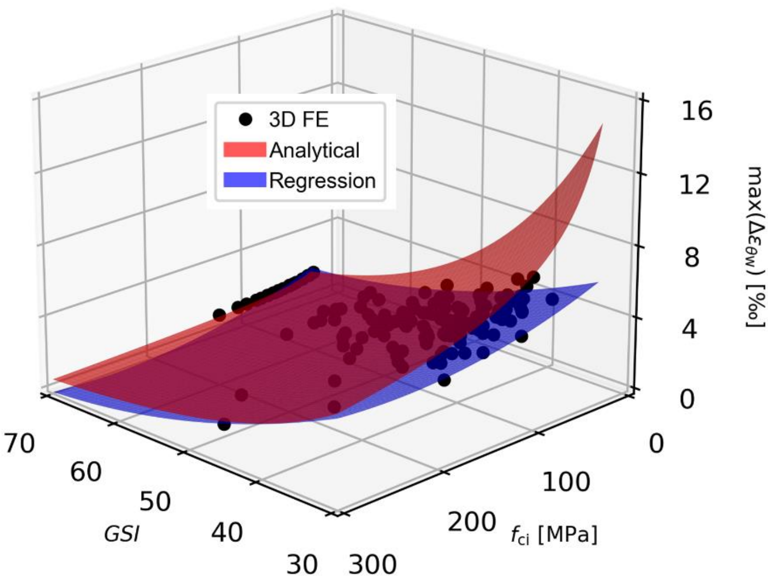

Regression model of 3D FE simulation results

$$\max(\Delta\varepsilon_{\theta \mathrm{w}}) = \frac{16}{10^3} - \frac{35GSI}{10^5} - \frac{24f_{\mathrm{ci}}}{10^{12}} + \frac{23GSI^2}{10^7} + \frac{5f_{\mathrm{ci}}^2}{10^{20}}$$

Figure 7.1. Results for the calculation of $\max(\varepsilon_{\theta \mathrm{w}})$ considering random variable inputs of GSI and f_{ci} for the 3D FE simulations, analytical model, and the regression model.

factor would be unpractical, requiring a large number of 3D FE simulations.

Performing a regression model directly on the results from 3D FE simulations could be a better approach, introducing less model error than the application of correction factors on the simplified analytical model. Figure 7.1 shows that a good fit of the results from the 3D FE simulations, with coefficient of determination of $R^2 = 0.97$, was obtained using a second order regression model without cross terms. Even if a good regression fit is achieved, the regression model estimations can still have a low accuracy especially for samples evaluated at distance from the 3D FE simulation results. Thus, regression models must be used carefully since they introduce an additional model error in the reliability-based analysis. A smaller model error could be introduced by using recorded sample evaluations throughout the limit state for new reliability-based analyses, as presented in Paper E. All recorded samples can be transformed from the physical space to the standard normal space using different input distributions for the random variable, and the probability of failure is then calculated using the RS method with DS method.

7.2.2. Considerations for advanced methods

Advanced reliability-based analysis was performed in this thesis by combining the ADIS method with 3D FE modeling of the LRC. Paper E showed that accurate results can be achieved by this approach, requiring only about $n_s = 10$ sample evaluations using 3D FE simulations. A logical structuration had to be created to automate the ADIS sampling from 3D FE simulations, and extensive computational programming was needed to implement it. The ADIS method was implemented using Python programming language, as well as the 3D FE simulation and post-processing of results from Abaqus v2020 (Dassault Systèmes Simulia Corp., 2019). All inputs were generated externally as text files so that the same reference scripts could be used for different reliability-based analyses. Deterministic inputs were kept the same; however, input files with mean values, coefficient of variations, distributions, and correlations were specified for each reliability-based analysis. A flowchart of the sampling procedure considered here is shown in Figure 3 of Paper E. Based on each random sample, rock mass properties were obtained and saved as input files for the FE analysis. The evaluated samples and performance responses are saved in a text file for each iteration in the ADIS method, which allows the reliability-based analysis to continue from the saved progress in case of error.

7.3. Compliance with safety requirement

The practical use of the advanced reliability-based approach proposed in Paper E is to ensure that societal safety requirements are met for the design of LRC gas storages. A target LRC design reliability considering high consequences of failure was set at a reliability index of $\beta_{\mathrm{ft}} = 5.2$ (probability of failure of $P_{\mathrm{ft}} = 10^{-7}$), based on the Eurocode (CEN, 2002). Possible solutions to comply with such safety requirements can be drawn based on the results of this work. In practice, field data and laboratory tests are needed to assist on the decision making.

7.3.1. Uplifting of the overburden

Paper D showed that a rock cover of $h_{\mathrm{ob}} \geq 105$ m would be sufficient for the LRC design in Skallen. These calculations used the analytical model from Eqs. (3.8)–(3.10), which give larger h_{ob} requirements compared to FE models (Papers A and D). Therefore, the rock cover of $h_{\mathrm{ob}} = 115$ m considered in the example based on Skallen conditions is more than sufficient for the LRC design. Uplifting of the overlying rock mass is avoided simply by placing the rock cavern deeper, so this is not considered to be a critical failure mode.

7.3.2. Ultimate straining of the steel lining

The maximum steel lining strains calculated in Papers B, E and in Figure 3.7b were smaller than the expected ultimate strain of the steel lining of $\varepsilon_{\mathrm{us}} \approx 15\%$. Only for an extreme scenario of very large concrete crack spacing, Figure 3.7b gave maximum strains larger than the ultimate strain of the reinforcement of $\varepsilon_{\mathrm{us}} \approx 5\%$. Since the aim of the reinforcement is mainly to redistribute strains close to the steel lining at maximum gas pressure, rupture of the reinforcement does not necessary lead to ultimate failure of the LRC.

The largest effect of opening of rock joints on the concentration of strains in the steel lining was observed in Paper B for "good" quality rock mass ($GSI = 70$), which should be the most susceptible geological conditions for ultimate failure of the steel lining. Conditions of "fair" quality rock mass can be expected to have smaller rock joint spacing, redistributing strains better, while "excellent" quality rock mass have smaller tangential strain at the rock cavern wall. The rock cavern wall must be sufficiently supported during the cavern excavation to prevent concentrated strains in the steel lining because of shear movement of rock blocks. Compaction at the rock cavern wall is expected during the first gas pressurization cycles, potentially increasing the Young's modulus of the rock mass. Smaller curvatures in the cavern geometry will further concentrate strains in the steel lining, so all corners should be rounded as much as practically possible.

In Paper B, a small spacing of rebars in the reinforcement with no relative movement between the concrete layer and steel lining resulted in the largest reductions of strain concentrations in the steel lining. However, the use of a sliding layer at the concrete-layer–steel-lining interface could be favorable to reduce the abrasion on the steel lining. Any fissures in the steel lining are locations where corrosion/hydrogen embrittlement are expected to develop. Hydrogen embrittlement could increase the steel strength properties but decrease the corresponding strain limits (Siddiqui and Abdullah, 2005). To reduce this effect, a steel with resistance to interaction with hydrogen may be needed in the steel lining. However, the effect of corrosion/hydrogen embrittlement on the LRC design have not been studied in detail here.

7.3.3. Fatigue of the steel lining

It was observed in Paper E that the reliability of the LRC design for fatigue of the steel lining is sensitive to the rock mass quality and its correlation with the unconfined compressive strength of the intact rock. It is expected that some degree of correlation exists between these parameters, which indicates that a mean value of $\mu_{GSI} \geq 75$ is required for the LRC design similar to Skallen. This conclusion is based on an LRC geometry where strain concentrations take place at the cavern invert (Paper E). If the cavern invert can be further smoothed, so that the maximum tangential strain range rather locates at the cavern mid-height, as in Paper A, a lower requirement of $\mu_{GSI} \geq 65$ is estimated based on Figure 3.6c. For this case however, the horizontal in-situ stresses have a larger influence on the maximum tangential strain at the mid-height cavern wall, and would also have to be considered to be random variables for the reliability-based design of the LRC.

In the long run, corrosion and hydrogen embrittlement may have an effect on the weld category in the steel lining, decreasing the value of $\mu_{f\mathrm{wc}}$ and increasing the variability $CV_{f\mathrm{wc}}$. Therefore, a steel material with resistance to corrosion and interaction with hydrogen should be considered for the steel plates in the LRC design.

8. Conclusions and suggestions for future work

8.1. Conclusions

The purpose of this thesis is to develop a reliability-based design tool for LRCs, to ensure that societal safety requirements and storage demands for fossil-free energy are met. Advanced FE models were used to achieve a more adequate representation of the actual LRC behavior, in combination with reliability-based approaches to address uncertainties and evaluate the LRC design reliability.

A reliability-based design tool for LRC gas storages was successfully developed. This tool was able to calculate small probabilities of failure for the LRC design to comply with societal safety requirements. Furthermore, this reliability-based design tool can, after validation with field data and laboratory experiments, be used in practice on, e.g., applications for LRC construction permits. Based on the research work performed in this thesis, the following conclusions can be drawn:

- Paper A showed that the derived analytical model for the response of the rock mass to the LRC gas pressurization gives reliable cavern wall tangential strain magnitudes for conditions of isotropic in-situ stresses and large cavern heights. This analytical model is inexpensive to evaluate and can be used to evaluate the reliability of the LRC design using the directional simulation (DS) method. For less idealized conditions, a 3D FE model gives a better prediction of the actual LRC behavior.

- In Paper B, the presented 2D FE model demonstrated the complex interaction between LRC components during gas pressurization and opening of rock joints at the rock cavern wall. The results showed that geological conditions of "good" quality rock masses ($GSI = 70$) have the largest influence of opening of rock joints on the strain concentrations in the steel lining, compared to "fair" quality and "excellent" quality rock masses. In addition, a well-reinforced concrete layer where no sliding of the steel lining is allowed gave the best setup for the reduction of concrete cracks. However, a sliding layer may still be needed to prevent damage on the steel lining surface because of high friction with the concrete layer.

- Regarding the suitability of calculation methods for the reliability-based design of LRCs, the subset simulation (SS) method (Paper C) was more efficient than the Monte Carlo simulation (MCS) method; however, still SS required a large number of samples to be used with FE models and had a large variability on the reliability estimations. The response surface (RS) method (Paper D) was more suitable to be used with FE models since it required a reasonably small number of samples and had a small variability on the reliability estimations. The combination of the DS and RS methods into the adaptive directional importance sampling (ADIS) method (Paper E) gave the best approach to perform reliability-based design of LRCs using computationally demanding FE models. For the ADIS method, only about $n_\mathrm{s} = 10$ sample evaluations were needed to estimate the reliability of the LRC design using $n_\mathrm{v} = 3$ random variables.

- In Paper E, the reliability-based analyses for fatigue of the steel lining using 3D FE models, with uncertainties related to the hard rock mass and steel lining, showed that the safety requirement of the LRC design was met for a mean rock mass quality represented by $\mu_{GSI} = 67$ (without $GSI{-}f_\mathrm{ci}$ correlation) and $GSI = 75$ (with high $GSI{-}f_\mathrm{ci}$ correlation). Corrosion and hydrogen embrittlement may however have a significant influence on the long-term structural reliability, but was not studied further within this work.

8.2. Suggestions for future work

The following future works are suggested based on the findings in this thesis:

- A more specific target probability of failure needs to be defined. The highest safety requirements defined in the Eurocode were used in this work; however, no specific guidelines are available for large underground gas storages;

- More field tests and laboratory experiments are needed to calibrate and further develop the present FE models.

- The characterization methods for probability distributions and spatial variabilities of uncertain properties in the rock mass, using geotechnical site investigations, need to be more clearly defined;

- The influence of the spatial variability of the geological conditions on the LRC design should be further investigated. Random fields can be used to model the uncertainties related to heterogeneous rock mass properties in more detail.

References

Alejano, L.R., Alonso, E., 2005. Considerations of the dilatancy angle in rocks and rock masses. Int. J. Rock Mech. Min. Sci. 42, 481-507. DOI: 10.1016/j.ijrmms.2005.01.003

Ang, A.H.S., Tang, W.H., 2007. Probability concepts in engineering: Emphasis on applications to civil and environmental engineering. Wiley, Ann Arbor, MI, USA

Au, S.K., Wang, Y., 2014. Engineering risk assessment with subset simulation. Wiley, Singapore, Singapore.

Baecher, G., Christian, J., 2003. Reliability and statistics in geotechnical engineering. John Wiley and Sons, Chichester, England.

Balla, A., 1961. The resistance to breaking out of mushroom foundations for pylons, Proceedings of the Fifth International Conference on Soil Mechanics and Foundation Engineering, Paris, France, pp. 569-576.

Baltay, P., Gjelsvik, A., 1990. Coefficient of friction for steel on concrete at high normal stress. J. Mater. Civil Eng. 2, 46-49. DOI: 10.1061/(ASCE)0899-1561(1990)2:1(46)

Basquin, O.H., 1910. The exponential law of endurance tests, Proceedings of the American Society for Testing Materials, pp. 625-630.

Bergman, T.L., Lavine, A.S., Incropera, F.P., Dewitt, D.P., 2011. Fundamentals of heat and mass transfer. John Wiley & Sons, Jefferson City, MO, USA.

Bieniawski, Z.T., 1989. Engineering rock mass classifications. Wiley, New York, NY, USA.

Bird, R.B., Stewart, W.E., Lightfoot, E.N., 2002. Transport phenomena, 2nd ed. John Wiley & Sons, Inc, Madison, WI, USA.

Bjureland, W., Johansson, F., Sjölander, A., Spross, J., Larsson, S., 2019. Probability distributions of shotcrete parameters for reliability-based analyses of rock tunnel support. Tunn. Undergr. Space Technol. 87, 15-26. DOI: 10.1016/j.tust.2019.02.002

Bjureland, W., Spross, J., Johansson, F., Prästings, A., Larsson, S., 2017. Reliability aspects of rock tunnel design with the observational method. Int. J. Rock Mech. Min. Sci. 98, 102-110. DOI: 10.1016/j.ijrmms.2017.07.004

Bourgeois, T., Ammouri, F., Weber, M., Knapik, C., 2015. Evaluating the temperature inside a tank during a filling with highly-pressurized gas. Int. J. Hydrog. Energy 40, 11748-11755. DOI: 10.1016/j.ijhydene.2015.01.096

Brown, E.T., Bray, J.W., Ladanyi, B., Hoek, E., 1983. Ground response curves for rock tunnels. J. Geotech. Eng. 109, 15-39. DOI: 10.1061/(ASCE)0733-9410(1983)109:1(15)

Cai, M., Kaiser, P.K., Tasaka, Y., Minami, M., 2007. Determination of residual strength parameters of jointed rock masses using the GSI system. Int. J. Rock Mech. Min. Sci. 44, 247-265. DOI: 10.1016/j.ijrmms.2006.07.005

Celestino, T.B., Aoki, N., Silva, R.M., Gomes, R.A.M.P., Bortolucci, A.A., Ferreira, D.A., 2006. Evaluation of tunnel support structure reliability. Tunn. Undergr. Space Technol. 21, 311. DOI: 10.1016/j.tust.2005.12.028

CEN, 2002. Eurocode - Basis of structural design, EN 1990:2002+A1. European Committee for Standardization, Brussels, Belgium.

CEN, 2005a. Eurocode 2: Design of concrete structures - Part 1-1: General rules and rules for buildings, EN 1992. European Committee for Standardization, Brussels, Belgium.

CEN, 2005b. Eurocode 3: Design of steel structures - Part 1-9: Fatigue strength, EN 1993. European Committee for Standardization, Brussels, Belgium.

Churchill, S.W., Chu, H.H.S., 1975. Correlating equations for laminar and turbulent free convection from a vertical plate. Int. J. Heat Mass Tran. 18, 1323-1329. DOI: 10.1016/0017-9310(75)90243-4

Cornelissen, H.A.W., Hordijk, D.A., Reinhardt, H.W., 1986. Experimental determination of crack softening characteristic of normal weight and lightweight concrete. HERON 31, 45-56. DOI:

Dassault Systèmes Simulia Corp., 2019. Abaqus v2020 software and documentation, Johnston, RI, USA.

Deák, I., 1980. Three digit accurate multiple normal probabilities. Numer. Math. 35, 369-380. DOI: 10.1007/BF01399006

DeGroot, D.J., Baecher, G.B., 1993. Estimating autocovariance of in-situ soil properties. J. Geotech. Eng. 119, 147-166. DOI: 10.1061/(ASCE)0733-9410(1993)119:1(147)

Diederichs, M.S., Kaiser, P.K., 1996. Rock instability and risk analyses in open stope mine design. Can. Geotech. J. 33, 431-439. DOI: 10.1139/t96-064

El-Ramly, H., Morgenstern, N.R., Cruden, D.M., 2002. Probabilistic slope stability analysis for practice. Can. Geotech. J. 39, 665-683. DOI: 10.1139/t02-034

fib, 2010. fib Model Code for Concrete Structures 2010. Wilhelm Ernst & Sohn., Lausanne, Switzerland.

Glamheden, R., Curtis, P., 2006. Excavation of a cavern for high-pressure storage of natural gas. Tunn. Undergr. Space Technol. 21, 56-67. DOI: 10.1016/j.tust.2005.06.002

Glamheden, R., Fredriksson, A., Röshoff, K., Karlsson, J., Hakami, H., Christiansson, R., 2007. Rock mechanics Forsmark - Site descriptive modelling - Forsmark stage 2.2, R-07-31. SKB Swedish Nuclear Fuel and Waste Management Co, Stockholm, Sweden.

Grooteman, F., 2011. An adaptive directional importance sampling method for structural reliability. Probabilist. Eng. Mech. 26, 134-141. DOI: 10.1016/j.probengmech.2010.11.002

Hoek, E., Brown, E.T., 1980. Underground excavations in rock. Taylor & Francis, Boca Raton, FL, USA.

Hoek, E., Carranza-Torres, C., Corkum, B., 2002. Hoek–Brown failure criterion - 2002 edition, Proceedings of the North American Rock Mechanics Symposium, Toronto, Canada, pp. 267-273.

Hoek, E., Diederichs, M.S., 2006. Empirical estimation of rock mass modulus. Int. J. Rock Mech. Min. 43, 203-215. DOI: 10.1016/j.ijrmms.2005.06.005

Hoek, E., Kaiser, P.K., Bawden, W.F., 1995. Support of underground excavations in hard rock. Balkema, Rotterdam, Netherlands.

Jing, Z., Yin, X., 2020. Neural network-based prediction model for passenger flow in a large passenger station: An exploratory study. IEEE Access 8, 36876-36884. DOI: 10.1109/ACCESS.2020.2972130

Johansson, F., Spross, J., Damasceno, D.R., Johansson, J., Stille, H., 2018. Investigation of research needs regarding the storage of hydrogen gas in lined rock caverns: Prestudy for work package 2.3 in HYBRIT research program 1, TRITA-ABE-RPT-182. KTH Royal Institute of Technology, Stockholm, Sweden.

Johansson, J., 2003. High pressure storage of gas in lined rock caverns: Cavern wall design principles, TRITA-JOB LIC 2004. KTH Royal Institute of Technology, Stockholm, Sweden.

Johansson, J., Stille, H., Sturk, R., 1995. Pilotanläggning för inklädda gaslager i Grängesberg - Fördjupad analys av försöksresultaten [Pilot plant for lined gas storage in Grängesberg - In-depth analysis of the experimental results], TRITA-AMI Report 3004. KTH Royal Institute of Technology, Stockholm, Sweden.

Kohno, S., Ang, A.H.S., Tang, W.H., 1992. Reliability evaluation of idealized tunnel systems. Struct. Saf. 11, 81-93. DOI: 10.1016/0167-4730(92)90001-4

Krounis, A., Johansson, F., Larsson, S., 2016. Shear strength of partially bonded concrete–rock interfaces for application in dam stability analyses. Rock Mech. Rock Eng. 49, 2711-2722. DOI: 10.1007/s00603-016-0962-8

Lacasse, S., Nadim, F., 1996. Uncertainties in characterising soil properties, Proceedings of the Offshore Technology Conference, Houston, TX, USA, pp. OTC-7996-MS.

Langford, J.C., Diederichs, M.S., 2013. Reliability-based approach to tunnel lining design using a modified point estimate method. Int. J. Rock Mech. Min. Sci. 60, 263–276. DOI: 10.1016/j.ijrmms.2012.12.034

Lee, J., Fenves, G.L., 1998. Plastic-damage model for cyclic loading of concrete structures. J. Eng. Mech. 124, 892-900. DOI: 10.1061/(ASCE)0733-9399(1998)124:8(892)

Lu, M., 1998. Finite element analysis of a pilot gas storage in rock cavern under high pressure. Eng. Geol. 49, 353-361. DOI: 10.1016/S0013-7952(97)00067-7

Lü, Q., Chan, C., Low, B., 2013. System reliability assessment for a rock tunnel with multiple failure modes. Rock Mech. Rock Eng. 46, 821-833. DOI: 10.1007/s00603-012-0285-3

Lubliner, J., Oliver, J., Oller, S., Oñate, E., 1989. A plastic-damage model for concrete. Int. J. Solids Struct. 25, 299-326. DOI: 10.1016/0020-7683(89)90050-4

Malm, R., 2006. Shear cracks in concrete structures subjected to in-plane stresses, TRITA-BKN. Bulletin 88. KTH Royal Institute of Technology, Stockholm, Sweden.

Malm, R., 2016. Guideline for FE analyses of concrete dams, 2016:270. Energiforsk, Stockholm, Sweden.

Mansson, L., Marion, P., Johansson, J., 2006. Demonstration of the LRC gas storage concept in Sweden, Proceedings of the 23rd World Gas Conference. International Gas Union, Amsterdam, Netherlands, pp. 404-420.

Melchers, R.E., Beck, A.T., 2018. Structural reliability analysis and prediction, 3rd ed. Wiley, Hoboken, NJ, USA.

Myers, R.H., Montgomery, D.C., Anderson-Cook, C.M., 2009. Response surface methodology: Process and product optimization using designed experiments. Wiley, Hoboken, NJ, USA.

NIST, 2022. National Institute of Standards and Technology, https://webbook.nist.gov, accessed 20/06/2022.

Olmos, F., Manousiouthakis, V.I., 2013. Hydrogen car fill-up process modeling and simulation. Int. J. Hydrog. Energy 38, 3401-3418. DOI: 10.1016/j.ijhydene.2012.12.064

Park, D., Kim, H.M., Ryu, D.W., Choi, B.H., Han, K.C., 2013. Probability-based structural design of lined rock caverns to resist high internal gas pressure. Eng. Geol. 153, 144-151. DOI: 10.1016/j.enggeo.2012.12.001

Phoon, K.K., 2008. Reliability-based design in geotechnical engineering: Computations and applications. Taylor & Francis, London, England.

Rosenblatt, M., 1952. Remarks on a multivariate transformation. Ann. Math. Stat. 23, 470-472. DOI: 10.2307/2236692

Siddiqui, R.A., Abdullah, H.A., 2005. Hydrogen embrittlement in 0.31% carbon steel used for petrochemical applications. J. Mater. Process. Tech. 170, 430-435. DOI: 10.1016/j.jmatprotec.2005.05.024

Spross, J., Gasch, T., Johansson, F., 2022. Implementation of reliability-based thresholds to excavation of shotcrete-supported rock tunnels. Georisk. DOI: 10.1080/17499518.2022.2046789

Stephansson, O., 1993. Rock stress in the Fennoscandian shield, in: Hudson, J.A. (Ed.), Comprehensive rock engineering. Pergamon, Oxford, England, pp. 445-459.

Stille, H., Johansson, J., Sturk, R., 1994. High pressure storage of gas in lined shallow rock caverns - Results from field tests, Proceedings of the Rock Mechanics in Petroleum Engineering. SPE/ISRM, Rotterdam, Netherlands, pp. 689-696.

Suresh, S., 1998. Fatigue of materials, 2 ed. Cambridge University Press, Cambridge, England.

Tengborg, P., Johansson, J., Durup, J.G., 2014. Storage of highly compressed gases in underground lined rock caverns - More than 10 years of experience, Proceedings of the World Tunnel Congress. ITA, Foz do Iguaçu, Brazil.

Vanmarcke, E.H., 1977. Probabilistic modeling of soil profiles. J. Geotech. Eng.-ASCE 103, 1227-1246. DOI: 10.1061/AJGEB6.0000517

Vattenfall Press Office, 2022. HYBRIT: Milestone reached - Pilot facility for hydrogen storage up and running, https://group.vattenfall.com/press-and-media/newsroom/2022/hybrit-milestone-reached--pilot-facility-for-hydrogen-storage-up-and-running, accessed 20/10/2022.

Vesic, A.S., 1971. Breakout resistance of objects embedded in ocean bottom. J. Soil Mech. Found.-ASCE 97, 1183-1205. DOI: 10.1061/JSFEAQ.0001659

Vezole, P., 2002. Ancrages passifs verticaux et calcul à la rupture [Passive vertical anchors and yield design theory]. Revue Francaise de Geotechnique 98, 47-62. DOI: 10.1051/geotech/2002098047

Waarts, P.H., 2000. Structural reliability using finite element analysis - An appraisel of DARS: Directional adaptive response surface sampling, 90-407-2073-8. Delft University Press, Delft, Netherlands.

Zeng, P., Senent, S., Jimenez, R., 2016. Reliability analysis of circular tunnel face stability obeying Hoek–Brown failure criterion considering different distribution types and correlation structures. J. Comput. Civ. Eng. 30, 04014126. DOI: 10.1061/(ASCE)CP.1943-5487.0000464